1526

Photopatterning of Thick Photoresist Layers for MEMS Applications

A dissertation submitted to the Faculty of Sciences of the University of Neuchâtel, in fulfilment of the requirements for the degree of "*Docteur ès Sciences*"

by

Sylvain Roth
Diplômé en électronique physique
de l'Université de Neuchâtel

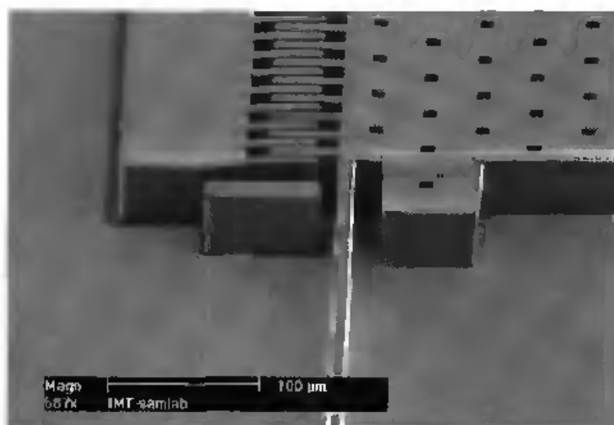

Institute of Microtechnology
University of Neuchâtel
Rue Jaquet-Droz 1, CH-2007 Neuchâtel
Switzerland

2000

For with you is the fountain of life;
In your light we see the light.

The Bible, Psalm 36 v. 10.

Car auprès de toi est la source de la vie;
Par ta lumière nous voyons la lumière.

La Bible, Psaumes 36 v. 10.

Contents

Chapter 1: Introduction 1

1.1. A brief history 1

1.2. Objectives and outline of this work 3

1.2.1. Objectives 3

1.1.2. Outline 4

1.3. References 5

Chapter 2: High Aspect Ratio UV Photolithography 7

2.1. Introduction 7

2.2. The Clariant AZ-4562 positive resist 9

2.3. Coating of thick resist layers 10

2.3.1. Introduction 10

2.3.2. Thick resist layer process sequences 11

2.4. Pre-baking of the thick resist layers 13

2.4.1. Introduction 13

2.4.2. Thick resist layer pre-bake sequences 14

2.5. UV light photopatterning and nickel electroplating............ 15

2.5.1. introduction.. 15

2.5.2. Rehydration time and edge-bead removal..................... 17

2.5.3. Exposure, development and postbake of the thick resist layers 19

2.5.4. Nickel electroplating.. 21

2.6. Results.. 24

2.6.1. Introduction.. 24

2.6.2. 38 μm thick resist moulds and nickel structures............. 24

2.6.3. 85 μm thick resist moulds and nickel structures............. 29

2.6.4. Discussion.. 36

2.7. Conclusion.. 38

2.8. References.. 39

Chapter 3: Applications of Thick Photoresist Patterning 41

3.1. Introduction 41

3.2. Protection of protruding structures during wet and dry etching processes 42

3.2.1. Introduction.. 42

3.2.2. Tips fabrication and thick photoresist patterning............ 42

3.2.3. Results 43

3.3. Electrostatic microfabricated gyroscope 46

3.3.1. Introduction.. 46

3.3.2. Macroscopic and micromachined gyroscopes................ 47

3.3.3. Working principle.. 51

3.3.4. FE modal analysis 51
3.3.5. Design considerations 54
3.3.6. Expected sensitivity 57
3.3.7. Fabrication process 59
3.3.8. Fabrication results 62
3.3.9. Characterisation 67
3.3.10. Conclusion 70
3.4. References 72

Chapter 4: Microfabricated Reed Relay 75

4.1. Introduction 75
4.2. Design 77
4.2.1. Working principle 77
4.2.2. Design considerations 78
4.3. Fabrication 79
4.3.1. Fabrication process 79
4.3.2. Process limitations 81
4.3.3. Fabrication results 86
4.4. Analytical model calculation 88
4.4.1. Magnetic reluctance 89
4.4.2. Magnetic reluctance equivalent circuit 90
4.4.3. Required magnetic force and flux 92
4.4.4. Required permanent magnet and coil magnetic field 94
4.4.5. Zero-gap magnetic force 95
4.4.6. Calculated value 96

4.5. Characterisation ... 97

4.5.1. Electrical resistance ... 97

4.5.2. Dynamic measurements ... 101

4.5.3. Self-test coil ... 104

4.5.4. Permeability ... 106

4.5.5. Design improvements ... 109

4.6. Conclusion ... 110

4.7. References ... 112

Chapter 5: Conclusion **115**

Acknowledgements **117**

Bibliography **119**

Chapter 1
Introduction

1.1. A BRIEF HISTORY

Photolithography was first developed for the quasi two-dimensional processes of microelectronics to transfer copies of a master pattern onto the surface of a solid material, such as silicon wafers. With the emergence of micromechanics, more interest was generated for three-dimensional processes. In the early 1950s, Robbins and Schwartz [1.1] developed the bulk isotropic etching of silicon with mixtures of HF and HNO_3. In the mid-1960s, the Bell Telephone Laboratories started work on anisotropic Si etching, initially in mixtures of KOH, water, and alcobol, and later in aqueous KOH solutions. These etching technologies opened the way to the 3-D micromachining of silicon. Bulk micromachining, which is used to etch into both crystalline and non-crystalline materials, is limited with respect to achievable structure geometries. This motivated the development of surface micromachining features in the early 1960s [1.2]. In this technique, structures are built up, layer by layer, on the surface of a substrate. Usually, dry etching defines the features in a thin surface layers and wet etching releases them from the bulk material underneath by undercutting. Surface micromachining as we know it today was first

demonstrated by Howe and Muller in the early 1980s, with polysilicon used as structural material [1.3].

Bulk and surface micromachining technologies only allow the realisation of deep grooves in the bulk and thin structures (a few microns) on the surface of planar substrates. In 1975, Romankiw and co-workers at IBM combined electrodeposition and X-ray lithography [1.4]. They made high aspect ratio metal structures by plating gold in up to 20 µm thick X-ray-defined resist patterns. In 1982, Ehrfeld presented the LIGA technique [1.5], which consists of a thick layer of resist (from microns to millimetres of poly(methylmethacrylate) (PMMA)) structured by high energy collimated X-ray radiation exposure and subsequently developed to obtain a three-dimensional resist mould. The resist mould is filled by electrodeposition with a metal and the 3-D standing metal structure is released by removing the resist. Typical values for LIGA features are heights of 20 to 500 µm, minimum dimensions of 1 to 2 µm and surface roughness of 0.03 to 0.05 µm [1.6]. The generation of X-ray radiation is complicated and expensive, requiring the use of a synchrotron source. The masks used in LIGA differ substantially from those for the standard IC industry. The main difference lies in the absorber thickness. Very thick absorbers (>10 µm of Au vs. 0.1 µm Cr) and highly transparent mask substrates must be used in order to achieve a high contrast (>200), because of the low resist sensitivity, the resist layer depth, and the high exposure dose (hundred times higher than in the IC case). The LIGA technology offers the advantages of very thick layers (up to mm) and very good surface roughness (less than 0.05 µm), but is still a very heavy and expensive technology. The construction costs of a typical synchrotron totals over 30 million Euro [1.6], restricting dramatically access to this technology. Since the advent of LIGA, an effort has been made to develop low-cost solutions, based on commonly available processes, that approximate LIGA results. This has motivated the development of different photolithography techniques for high aspect ratio

structures. M. G. Allen [1.7] fabricated plating moulds using photosensitive polyimide in conjunction with UV exposure. Several groups fabricated high aspect ratio moulds for metal electroplating with photolithography [1.8, 1.9, 1.10], using commercially available highly viscous positive photoresist (Clariant AZ-4000 family) and near-UV light source. In the mid-1990's, IBM developed SU-8, a negative epoxy-based resist with a very low absorption coefficient [1.11]. High aspect ratios (>10) and straight sidewalls in thick layers (>500 μm) are possible by applying standard lithography. The most problematic aspect of this resist is the stripping and the residual stress in the layer. This type of new high aspect ratio resist process has encouraged further developments of inexpensive LIGA-like technologies in the micromachining community.

1.2. OBJECTIVES AND OUTLINE OF THIS WORK

1.2.1. Objectives

The main objective of this Ph.D. Thesis is to demonstrate the suitability of the thick photoresist layers photopatterning for MEMS applications. In order to define a range of applications, for which the presented technology is a good alternative to LIGA, the limits and the advantages of the fabrication process are presented. Thick resist patterning technology combined with metal (nickel for instance) electrodeposition has the advantage to be fully IC compatible and allows to integrate mechanical structures directly onto an IC circuit [1.12]. The thick resist technology is a low cost fabrication process with some advantages over other standard 3D-microfabrication techniques. A gyroscope and a reed relay have been microfabricated to demonstrate the suitability of the thick resist technology for MEMS devices fabrication.

1.2.2. Outline

The present chapter is a brief introduction explaining the interest of the development of thick photoresist moulds process. It gives the objectives and the outline of this work.

Chapter 2 explains each steps of the fabrication process for 38 µm, 55 µm and 85 µm thick Clariant AZ 4562 resist moulds. Some critical parameters are highlighted and all parameters values are given for the optimised process. Results and process limitations are also discussed.

Chapter 3 starts with enumerating different devices developed in our laboratory, which have required, for their fabrication, one of the thick resist fabrication process presented in Chapter 2. Protection of protruding structures during wet and dry etching processes with thick photoresist layers is then discussed. Finally, a long section describes the working principle, the design, the simulation with finite elements analysis, the fabrication and the characterisation of a vibrating tuning fork gyroscope, fabricated with the thick resist technology. Sacrificial layers related problem and mass sticking problem are also briefly discussed.

Chapter 4 describes the working principles, the design, the fabrication and the characterisation of reed relay for position detection applications. The fabrication has been realised with thick resist mould technology. The proposed relay is actuated by magnetic forces, includes a self-test function, requires a single photolithography step and is mounted into a Surface Mounted Device (SMD) package.

Chapter 5 is the final conclusion, which highlights the work performed in this Ph.D. thesis.

1.3. REFERENCES

[1.1] H. R. Robbins and B. Schwartz, "Chemical etching of silicon-I. The system, HF, HNO_3 and H_2D", J. Electrochem. Soc., 106, 1959, pp. 505-508.

[1.2] H. C. Nathanson, W. E. Newell, R. A. Wickstrom and J. R. Davis, "The resonant gate transistor", IEEE Trans. Electron. Devices, ED-14, 1967, pp. 117-133.

[1.3] R. T. Howe and R. S. Muller, "Polycrystalline silicon micromechanical beams", Spring Meeting of the Electrochemical Society, Montreal, Canada, 1982, pp. 184-185.

[1.4] E. Spiller, R. Feder, J. Topalian, E. Castellani, L. Romankiw, and M. Heritage, "X-ray lithography for bubble devices", Solid State Technol., April, 1976, pp. 66-68.

[1.5] E. W. Becker, W. Ehrfeld, D. Munchmeyer, H. Betz, A. Heuberger, S. Pongratz, W. Glashauser, H. J. Michel and V. R. Siemens, "Production of separation nozzle systems for uranium enrichment by a combination of X-ray lithography and galvanoplastics", Naturwissenschaften, 69, 1982, pp. 520-523.

[1.6] M. Madou, "Fundamentals of microfabrication", CRC Press, 1997, pp. 275-323.

[1.7] M. G. Allen, "Polyimide-based process for the fabrication of thick electroplated microstructures", Tech. Dig. 7th Int. Conf. Solid-State Sensors and Actuators, Yokohama, Japan, 1993, pp. 60-65.

[1.8] E. W. Becker, W. Ehrfeld, P.Hagmann, A. Maner, D. Münchmeyer, Microelectronic Engineering, 1986, p. 435.

[1.9] G. Engelmann, O. Ehrmann, J. Simon and H. Reichl, "Fabrication of high depth-to-width aspect ratio microstructures", Proceedings. IEEE Micro Electro Mechanical Systems, (MEMS'92), Travemünde, Germany, 1992, pp. 93-98.

[1.10] B. Löchel, A. Maciossek, H.-J. Quenzer and B. Wagner, "UV depth lithography and galvanoforming for microfabrication", 186th Meet. Electrochem. Soc., Miami Beach, FL, 1994, pp. 100-111.

[1.11] K. Y. Lee, N. LaBianca, S.A. Rishton, S. Zolgharnain, J.D. Gelorme, J. Shaw and T.H.P Chang, "Micromachining Applications of a high resolution ultrathick photoresist",J. Vac. Sci. Technol. B 13, 1995, pp. 3012-3016.

[1.12] D.R. Sparks, S.R. Zarabadi, J.D. Johnson, Q. Jiang, M. Chia, O. Larsen, W. Higdon, P. Castillo-Borelley, " A CMOS integrated surface micromachined angular rate sensor: it's automotive application", Digest of Technical Papers 9th Internat. Conf. on Solid-State Sensors and Actuators, TRANSDUCERS '97, Chicago, USA, 1997, pp. 851-854.

Chapter 2
High Aspect Ratio UV Photolithography

2.1. INTRODUCTION

These last few years, many papers have been published contributing to a better understanding or to a significant improvement of thick positive photoresist moulds fabrication process used for metal electrodeposition. The development of spin-coaters with a co-rotating cover has enabled to coat thicker and more uniform photoresist layers [2.1]. Resist layers up to 100 μm and more have been spin coated during one single step. *Loechel et al.* have investigated three baking procedures for two different positive tone photoresists (AZ4562 and ma-P 100): air-forced oven, ramped hot-plate and infrared radiation (IR) [2.2]. They have shown that IR baking was advantageous compared to the other methods with respect to process duration and energy consumption. Compared to edge steepness, resolution edge loss, and surface roughness, all methods have delivered nearly identical results.

Conédéra et al. proposed in [2.3], a method to optimise the photolithography step for 43 μm and 63 μm thick resist layers. The technique was based on the measurement of the photoresist transparency variation during exposure. With

this method, optimised parameters for the prebake (temperature and duration) and for the room relative humidity have been obtained.

In thick pbotoresist printing, the resist thickness can easily be larger than the mask/wafer gap. The resist is thus pattemed like standard prints at large gaps. For very thick photoresist layers the influence of diffraction effects results in a typical line shape: inclined side walls. Large exposure gap optics (LEGO, Süss, Germany), have been developed to reduce the undesired diffraction effects [2.4, 2.5]. Vacuum contact exposure mode has also been reported to reduce diffraction effects and to improve pattem definition [2.6].

The fabrication of resist moulds for metal plating generally requires a post-bake step to improve the chemical resistance to the plating solution. However, postbakes have been reported to cause pattem distortion, which can be unacceptable for certain applications [2.7].

This short overview shows the importance of each fabrication step of the thick photoresist mould technology. Any parameter change could alter the final result. This chapter describes single and double layer processes to make thick resist moulds of Clariant AZ-4562 (38 µm, 55 µm 85 µm) with good reproducibility. The pattemíng of the thick photoresist layers was performed with standard photolithography equipment. Different problems related to thick photoresist pattemíng, such as edge beading and resist cracking, are discussed and solutions proposed. Side walls are characterised after nickel electrodeposition. Results and process limitations are presented.

2.2. THE CLARIANT AZ-4562 POSITIVE RESIST

The Clariant AZ-4562 positive photoresist is a two-components formulation made of a polymer base, novolac resin (N), and a photosensitizer, diazonaphthoquinone (DQ) [2.8]. When a hydrophobic DQ is added to an alkali-soluble resin (N), the resin dissolution is inhibited (Fig. 2.1).

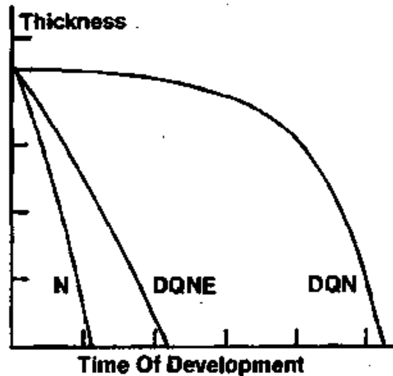

Fig. 2.1: Thickness versus time of development of novolak (N) film, diazonaphthoquinone mixed with novolak (DQN), and exposed diazonaphthoquinone in novolak (DQNE). From M. W. Moreau, "Semiconductors lithography principles, practices, and materials", Plenum Press New York7, 1988, pp. 3.

During the photolysis (Fig. 2.2), the DQ generates a carbene (C) which rearranges to a ketene (K). The ketene reacts with absorbed moisture present in the resin to form an indene acid (A). The photochemical destruction of the inhibitor and the release of uncomplexed resin induce, upon development in an alkali solution, the dissolution of the exposed resist.

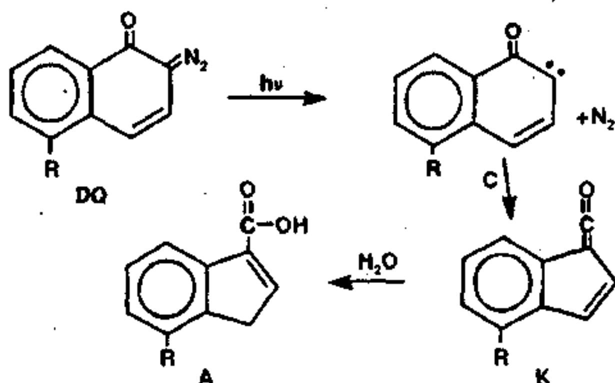

Fig. 2.2: Photolysis of the photosensitizer (DQ) into an indene acid (A), soluble in an alkali solution. From M. W. Moreau, "Semiconductors lithography principles, practices, and materials", Plenum Press New York, 1988, pp. 35.

2.3. COATING OF THICK RESIST LAYERS

2.3.1. Introduction

The thickness of a resist layer is determined by the resist properties (e.g. viscosity) and the spin coating speed: the slower the speed, the thicker is the coated resist layer. As reported by *Miyajima* and *Mehregany* [2.9], a non-uniform coating is observed when the coating speed is too slow. Thereby, for contact or vacuum contact exposure modes, the contact between the mask and the wafer is not uniform enough to obtain high pattern resolution. The *Gyrset RC8* (*Karl-Süss, Germany*) spin coater with a co-rotating cover (Fig. 2.3) allows the fabrication of thicker and more uniform resist layers in one single coating step. The solvent saturated and co-rotating atmosphere created by the Gyrset system avoids the drying of the resist and improves the resist layer homogeneity [2.4].

Fig. 2.3: RC8 spin-coater with co-rotating cover. The co-rotating cover allows the deposition of thicker and more uniform resist layers in one single coating step.

Three resist layer thickness processes (38 µm, 55 µm and 85 µm) were developed, taking into account in particular:

- process simplicity (with maximum two coating steps).
- minimisation of the width of peripheral region where edge-beading takes place, in order to maximise the useful wafer area.
- thickness uniformity.

2.3.2. Thick resist layer coating process sequences

38 µm thick resist layer process

The developed spinning sequence to coat 38 µm thick resist layers consists in a 30 seconds long step at 110 rpm (Fig. 2.4). The accumulation of resist (edge beading) at the edge of the substrate prevents a good contact between the mask and the resist during the exposure step, decreasing the precision of the

patterning (see § 2.5). The long spinning time [2.1] and the presence of a short and strong acceleration (2000 rpm/s) in the middle and at the end of the spinning sequence reduce the width of the region in which the edge-beading takes place. The spinning sequence developed for the 38 μm thick layer process has been used as the basis for the development of the two other thicker layer processes.

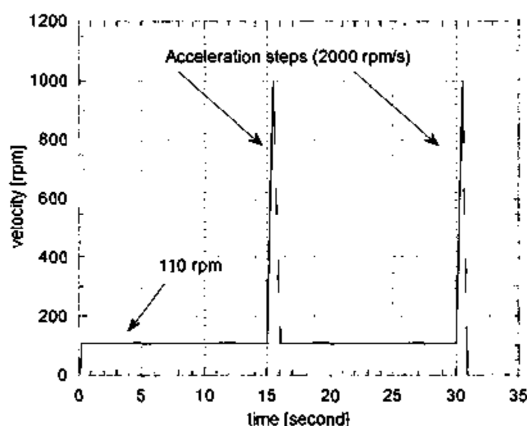

Fig. 2.4: Spinning sequence to achieve 38 μm thick resist layers. The introduction of a short and strong acceleration (2000 rpm/s) in the middle and at the end of the spinning sequence reduces the edge-beading effects.

The 85 μm thick resist layer process

To obtain the 85 μm thick resist layer, the 38 μm spinning sequence is performed twice with a short pre-bake in between. The final thickness is not the sum of two single coats of photoresist (i.e. 38+38 ≠ 85). According to [2.9], the adhesion of the second resist layer to the first is better than the first to the substrate, resulting in a greater thickness than expected.

The 55 μm thick resist layer process

To obtained the 55 μm thick resist layer, a 6.8 μm resist layer is first spun (1000 rpm during 3 seconds then 4000 rpm during 40 seconds) without the co-rotating cover, followed by the 38 μm sequence without any pre-bake in between. As for the 85 μm sequence, the first thin resist layer acts as an adhesion layer for the second one.

2.4. PRE-BAKING OF THE THICK RESIST LAYERS

2.4.1. Introduction

Prebake, also known as softbake or pre-expose bake, is the physical process of conversion of a liquid resist layer into a solid film. In the prebake step, the most of the solvent is evaporated without the degradation of the resist components. Because of the relatively high boiling point of the solvent (>130°C), there will always remain a small amount of solvent left in the dried resist.

Since the pre-bake process can have an effect on subsequent processes such as exposure and development, the pre-bake is the most critical step of the thick resist process, and should be precise, uniform across the wafer, and reproducible. If the pre-bake temperature is too high, the photosensitive component may be partially degraded, and higher dose will be required for the exposure step. If it is too low, the solvent may interfere with the photolysis reaction, and different exposure-development parameters may be required. In fact, it influences the required exposure energy and development time, the structure resolution, the mould's side walls and aspect ratio [2.10].

To allow efficient evaporation of the solvent, the pre-bake is done on a ramped hotplate in a nitrogen environment. The heat input from the rear side of the wafer prevents crust formation at the top surface of the resist [2.11]. When the substrate is put in direct contact with the hotplate at bake temperature, the

thick resist tends to flow to the centre of the wafer. This phenomenon can be avoided by a programmed temperature ramp.

2.4.2. Thick resist layer pre-bake sequences

The 38 µm baking sequence is a temperature ramp from 40 to 90° C during 15 minutes followed by a 60 minutes plateau at 90° C. The 55 µm baking sequence is a temperature ramp from 40° to 90° C during 10 minutes followed by a 90 minutes plateau at 90° C. The 85 µm baking sequence involves two bakes. The first bake is performed after the coating of the first resist layer and consists in a 3 minutes ramp from 40° to 80° C followed by a 10 minutes plateau at 80° C. The second bake is performed after the coating of the second resist layer and consists in a 15 minutes long ramp from 40° to 90° C and followed by a 150 minutes plateau at 90° C. Table 2.1 summarises the different pre-baking parameters for the three layer thicknesses.

Layer Thickness	Starting Temperature	Final Temperature	Ramp Duration	Plateau Duration
38 µm	40° C	90° C	15 minutes	60 minutes
55 µm	40° C	90° C	10 minutes	90 minutes
85 µm first	40° C	80° C	3 minutes	10 minutes
85 µm second	40° C	90° C	15 minutes	150 minutes

Table 2.1: Summary of the pre-bake parameters for the different layer thicknesses.

2.5. UV LIGHT PHOTOPATTERNING AND NICKEL ELECTROPLATING

2.5.1. Introduction

The positive AZ family of photoresists is sensitive to UV light. A mercury lamp is generally used as light source. For proper operation the light energy must be absorbed by the diazonaphthoquinone (DQ) photoactive compound which, when exposed, is converted into soluble indene carboxylic acid (E) (Fig. 2.5).

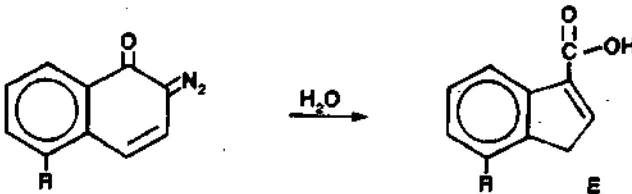

Fig. 2.5: Photolytic conversion of the photosensitizer (DQ) into an indene acid (E), soluble in an alkali solution. From M. W. Moreau, "Semiconductors lithography principles, practices, and materials", Plenum Press New York, 1988, pp. 488.

One molecule of water per molecule of DQ is required to ensure this conversion [2.12]. If water is missing, the DQ will crosslink to an insoluble compound (Fig. 2.6), and exposed areas will not dissolve in developer.

As the necessary water is not contained in the resist layer, a rehydration time is necessary to let the moisture being absorbed from the atmosphere (see section 2.5.2). For this reason, photolytic conversion of DQ to E will drastically fall off if humidity is below 30% RH. If the upper limit for humidity goes above 60% RH, the resist layer will absorb too much water, resulting in adhesion problems. For these reasons, a relative humidity of 45% is recommended. Exposed areas of resist are dissolved during development. Developers are aqueous alkaline solutions either based on sodium hydroxide (inorganic

developers) or Tetra Methyl Ammonium Hydroxide TMAH (organic developers). The Clariant AZ-400K developer used in this process is based on NaOH hydroxide and buffered by borate. The temperature itself is not critical and room temperature is used (20 - 25 °C), however, it should be kept constant (±1 °C) for best process reproducibility.

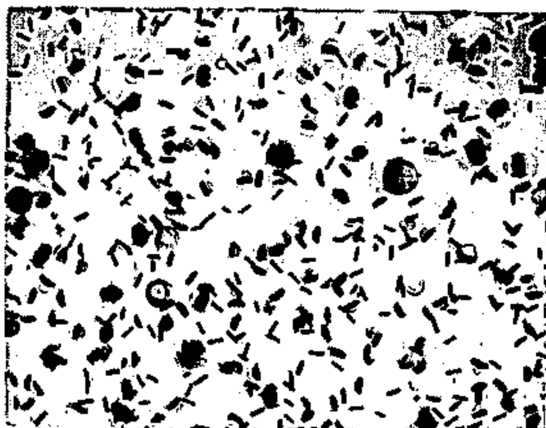

Fig. 2.6: DQ crosslinking to an insoluble compound (black dots), due to lack of water during exposure.

The main difficulties in photopatterning thick resist layers with UV light are exposing the entire resist thickness, obtaining a maximum mould verticality, keeping a good pattern definition and avoiding resist peeling and cracking.

Different simple "tricks" can address these problems:

- A high exposure energy assures the illumination through the entire resist layer [2.3] and improves the mould edge slope by reducing the required development time.
- Vacuum contact exposure mode improves pattern definition and moulds edge slope by reducing the diffraction effects over a larger

area, compared to the hard-contact mode [2.9, 2.5, 2.6]. However, an edge-bead removal step is then necessary to establish a good vacuum contact between the mask and the resist layer.

- Resist peeling appears after long exposition times, due to the formation of nitrogen gas as the resist photoactive component reacts [2.13]. Increasing the resist pre-baking reduces this phenomenon [2.14].

- In order to avoid layer cracking during the edge-bead removal, during the exposure and the development steps, a relaxation time for resist rehydration is performed between the pre-bake and the resist exposure.

2.5.2. Rehydration time and edge-bead removal

Before the UV exposure, a rehydration step is performed, followed by edge-bead removal. The rehydration time strongly depends on the room temperature and humidity. Table 2.2 presents the optimum rehydration time values determined experimentally for a room temperature of 21°C ± 2°C and a room humidity of 45% ± 2%. The rehydration step also permits the reduction of the exposure energy and the development time. A decrease in the latter helps to reduce the dissolution (by the developer) of unexposed resists regions.

Layer Thickness	Rehydration Time
38 µm	60 minutes
55 µm	150 minutes
85 µm	5 hours

Table 2.2: Optimum values of rehydration times determined experimentally for each layer thickness.

Fig. 2.7 shows a graph where the square root of the rehydration time (Table 2.2) is plotted vs. the layer thickness. The data points are distributed linearly, as predicted by the Einstein-Smoluchowski equation [2.15], expressing the distance travelled by diffusing molecules (Equation 2.1).

$$x = \sqrt{2Dt}$$ *Equation 2.1*

Where: *x: distance of the diffusion [cm].*
D: diffusion coefficient [cm²/s].
t: duration of the diffusion [s].

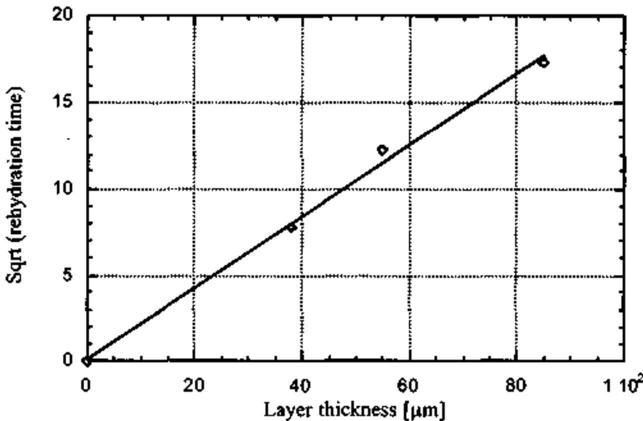

Fig. 2.7: Square root of the rehydration time vs. layer thickness

These results demonstrate that water diffuses into the resist layer during the rehydration time. At the end of the rehydration step, water is present throughout the layer, having had time enough to diffuse a distance equivalent to the thickness of the resist layer. The observation that exposure energy and development times are reduced when optimised rehydration times are applied, is a further evidence of this. Clearly, if the photolytic conversion of DQ to E is to be optimum, water must be present everywhere in the resist. Only then would it be possible to reduce both energy and development times. This model also

allows the prediction of the rehydration times necessary for different resist thicknesses, hence speeding up process optimisation.

The rehydration step is followed by the edge bead removal. It is performed by spinning the substrate at low velocity (500 rpm) and by spraying acetone with a syringe along the edge of the spinning wafer.

2.5.3. Exposure, development and postbake of the thick resist layers

Process parameters

The exposure is performed with a mask aligner (Electronic Vision AL6-2, mercury lamp 355 nm, 405 nm and 436 nm) in vacuum contact mode. Development is carried out with Clariant AZ 400K developer (one part of the developer diluted in four parts of de-ionised water). The wafer is immersed and then energetically agitated in the bath to enhance developer penetration into the small mould patterns. Table 2.3 shows the exposure and development parameters for the 38 µm, the 55 µm and the 85 µm thick resist layers on substrates with a metallic layer.

It has been noticed that for thick resist layers which are spun onto silicon, silicon dioxide or silicon nitride layers, the exposure energy has to be reduced. The long exposure time generates local peeling of the photoresist. This phenomenon seems to be related with adhesion problems [2.13], i.e. positive photoresists have a better adhesion on metallic layers than on silicon "family" layers. HMDS primer treatment doesn't significantly improve the thick resist layer adhesion. The last row of Table 2.3 gives the exposure and the development parameters for coating on non-metallic layer. The concentration of the developer is also changed (one part of the developer diluted in three parts of de-ionised water) to compensate the exposure energy decrease.

Layer thickness	Exposure energy	Development time	Developer concentration
38 µm	3500 mJ/cm^2	4 minutes	1:4
55 µm	2500 mJ/cm^2	8 minutes	1:4
85 µm	4750 mJ/cm^2	10 minutes	1:4
38 µm (non-metallic layers)	650 mJ/cm^2	4 minutes	1:3

Table 2.3: Exposure and development parameters for 38 µm, 55 µm and 85 µm thick resist layers on substrates with a metallic layer, and for 38 µm thick resist layers on non-metallic layers.

For electroplating application no post-bake is done after the development step, in order to avoid deformation of the resist mould [2.7]. If thick resist layers are used as protective layers for etching processes, a post-bake step of 15 min at 120°C on the hotplate is performed to stabilise the photo-resist and to avoid degassing during dry etching [2.16 and Chapter 3].

Influence of the rehydration time on the exposure and development parameters

The introduction of a rehydration time allows the reduction of the required exposure energy and the development time. As the developer also dissolves the unexposed resist regions, reduction of the development time improves the edge-slope of the moulds. Table 2.4 gives some development time values for different rehydration times for the 38 µm thick resist layer process.

Rehydration time	Exposure energy	Development time
about 20 minutes	3500 mJ/cm^2	12 minutes
about 45 minutes	3500 mJ/cm^2	6 minutes
about 60 minutes	3500 mJ/cm^2	4 minutes

Table 2.4: Influence of the rehydration time on the development time for the 38 μm process.

The Table 2.4 shows that when the quantity of water present in the resist layer is not sufficient, the photolytic conversion of DQ to E will drastically fall off, and by the way the development time is increased.

2.5.4. Nickel Electroplating

The wafer to be plated, with a metallic seed layer and with a photoresist mask defining the regions onto which nickel is to be deposited, is maintained at a negative potential (the cathode) relatively to the positive counterelectrode (the anode). The electroplating solution contains a reducible form of Ni ions. By biasing the surface to be plated with a negative potential, electrons are supplied to the surface of the exposed seed layer and Ni ions in the solution are reduced at the surface, resulting in nickel deposition.

The nickel electrodeposition reaction at the cathode, given in Equation 2.2, competes with the hydrogen reaction at the same electrode, in Equation 2.3.

$$Ni^{2+} + 2e^- \rightarrow Ni \qquad \textit{Equation 2.2}$$

$$2H^+ + 2e^- \rightarrow H_2 \qquad \textit{Equation 2.3}$$

The amount of hydrogen evolving and competing with Ni deposition depends on the pH, the temperature, and the current density. Since one of the most important causes of defects in the nickel microstructures is the appearance of hydrogen bubbles, these three parameters need precise control.

Impurities cause hydrogen bubbles to cling to the photoresist mould, resulting in pores in the deposited nickel layer. Therefore, the bath must be kept clean by circulating through a membrane filter. The main impurities are nickel hydroxide formed at increased pH-values in the cathode vicinity and organic decomposition products from the wetting agent. These problems can be avoided by monitoring and controlling the pH and by adsorbing the organic decomposition products on activated carbon.

Before the nickel electroplating process, the substrate with the thick photo-patterned resist moulds is dipped briefly in a 5% hydrochloric acid solution, to remove any oxide or organic impurities on the seed layer surface. A short dip into a wetting agent (Lea Ronal Wetting Agent) is also performed to improve the penetration of the plating bath into the very small structures of the mould. An illustration of poor wetting can be seen in Fig. 2.8, where the nickel solution didn't penetrate completely into the mould. By dipping the mould into the wetting agent before plating, the formation of the nickel structures was improved (Fig. 2.9).

The nickel sulfamate bath composition, optimised for nickel electrodeposition, is a commercial product (Nickel Sulfamate type from Lea Ronal). The bath is operated at 55°C and at a pH value between 3.8 and 4.5. Metal deposition is carried out at current densities of 1 to 2 A / dm^2.

The metal electroplating had to be performed within a day following the photoresist mould fabrication. After 24 hours, the mould deformation increases during the electrodeposition. This phenomenon is due to the hydration of the photoresist, which seems to weaken the photopatterned moulds.

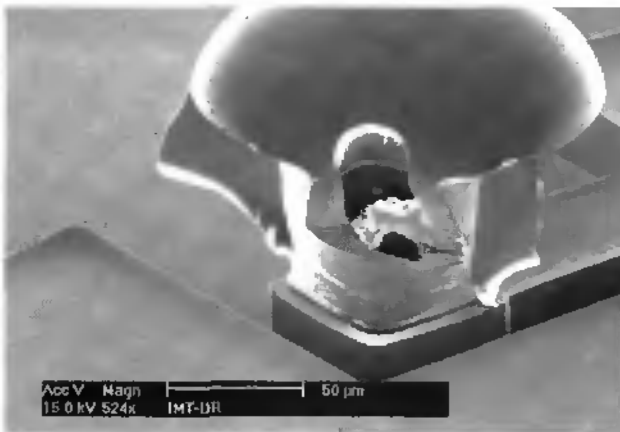

Fig. 2.8: The nickel solution didn't penetrate completely into the resist mould, resulting in a hole in the centre of the nickel structure, due to the presence of air.

Fig. 2.9: By using wetting agent, the formation of the nickel structures was improved.

2.6. RESULTS

2.6.1. Introduction

Results specifically related to particular applications are presented in Chapter 3 and Chapter 4. Some of the 55 µm thick layer photopatterning process limitations are presented in Chapter 4. In this section, general results and process limitations of the 38 µm and the 85 µm thick photoresist moulds fabrication are presented. Many of these presented results were obtained after nickel electrodeposition and mould dissolution in acetone, as most of the applications, for which the thick resist photopatterning processes were developed, are directly related to nickel devices.

2.6.2. 38 µm thick resist moulds and nickel structures

The 38 µm thick resist layer photo-patterning process is the most optimised process from the three which were developed. The reproducibility of the mould fabrication process was observed to be very good over the entire wafer (as long as the temperature and humidity of the room were stable around 21 ± 2° and 45% ± 2%).

38 µm thick resist moulds

Fig. 2.10 shows a SEM picture of a structure made in 38 µm thick resist. The dimensions of the square on the mask were 20 µm x 20µm. The over-development of the resist reduced the dimension to 14 µm at the bottom and 12 µm at the top of the resist structure. The side walls are well defined over the whole height.

Fig. 2.11 shows a 38 µm thick resist mould with a cylindrical hole of 10 µm diameter. The resist top surface is uniform

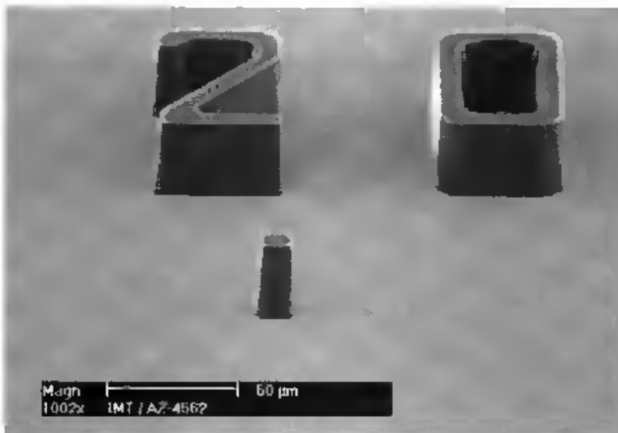

Fig. 2.10: SEM picture of a 13 µm (in the middle) wide square resist column.

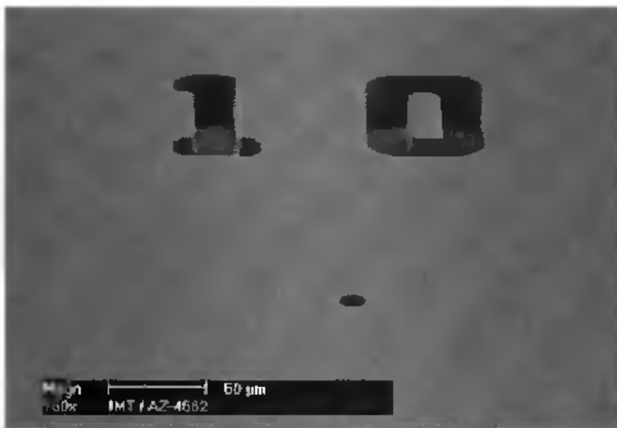

Fig. 2.11: SEM picture of hollow resist cylinder of 10 µm in diameter.

Fig. 2.12 shows a test structure used to evaluate the exposure and the development parameters by optical measurements. It consists of two parallel scales constituted of open lines on one side and filled lines on the other one. The reference position is defined by the central pair of open and filled lines, which have the same width on the mask. The over or under sizing of the structure

after development is measured by counting the shift, from the reference lines, of the pair having the same width. Each shift corresponds to an enlargement or a reduction of 1 μm per line edge. In this case, a reduction of 4 to 5 μm is measured between the mask patterns and the top of the resist mould.

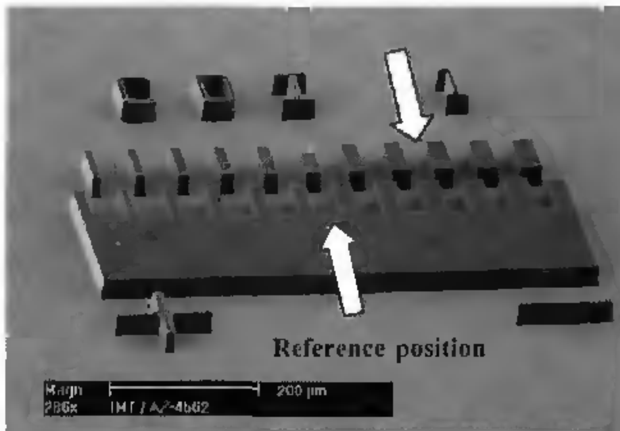

Fig. 2.12: SEM picture of a resist test structure used to define the enlargement between the resist and the mask patterns. A reduction of 4 to 5 μm is observed.

38 μm thick nickel structures

Fig. 2.13 shows a SEM picture of a 40 μm high and 14 μm in diameter nickel cylinder. The "mushroom" like appearance is due to nickel overgrowth in the mould. The definition of the mould wall is not so good at the top as at the bottom. This can be explained as a problem of light diffraction during exposure, which generally affects the upper 20% of the resist thickness [2.5]. The edges of the structure are measured close to 90°.

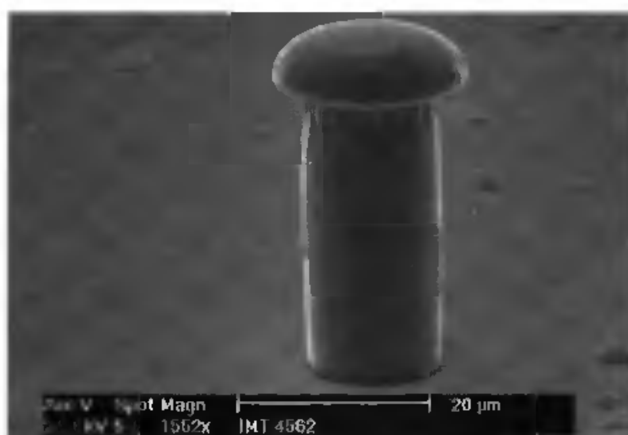

Fig. 2.13: SEM picture of a 40 µm thick and 14 µm in diameter nickel cylinder. The mushroom shape is due to the nickel overgrowth.

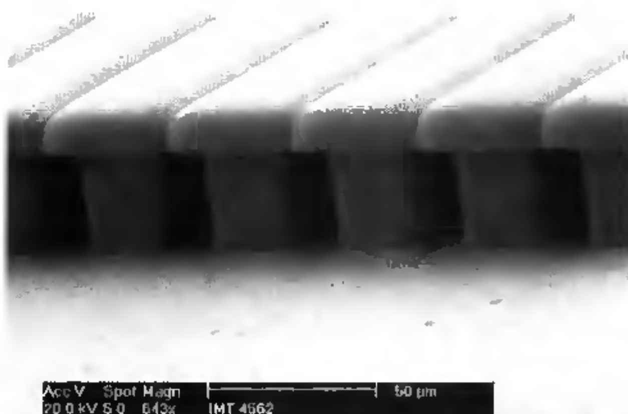

Fig. 2.14: SEM picture of a nickel lattice. Lines and spaces width is 24 µm and 16 µm respectively

Fig. 2.14 shows a SEM picture of a nickel lattice of 24 µm wide lines and 16 µm wide spaces (20 µm and 20 µm respectively on the mask). Despite the long baking sequence, no photoresist rest is observed. Although the nickel

overgrowth makes the observation of the whole structure impossible, it can be assumed that the resist has been completely dissolved in acetone.

Fig. 2.15 shows a nickel comb test structure used to determine the smallest lateral distance between two opposite comb fingers (gap). On the mask, the finger width is 4 µm and the gaps vary from 4 µm to 10 µm. Due to the mould enlargement, the realisation of nickel combs with final gap sizes smaller than 2 µm becomes very difficult.

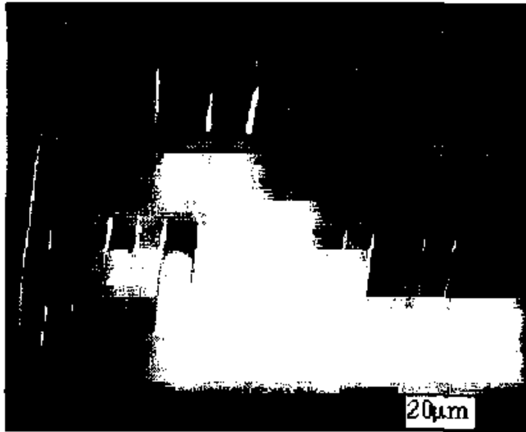

Fig. 2.15: SEM picture of a nickel comb like test structure with different gap sizes. The smallest measured gap of the nickel structure is 1.3 µm

Fig. 2.16 shows a front view of the smallest nickel line realised with the 38 µm thick mould process. The line pattern is 1 mm long and 2 µm wide on the mask. The measured width is 7 µm. The mushroom-like appearance is due to a nickel overgrowth in the mould.

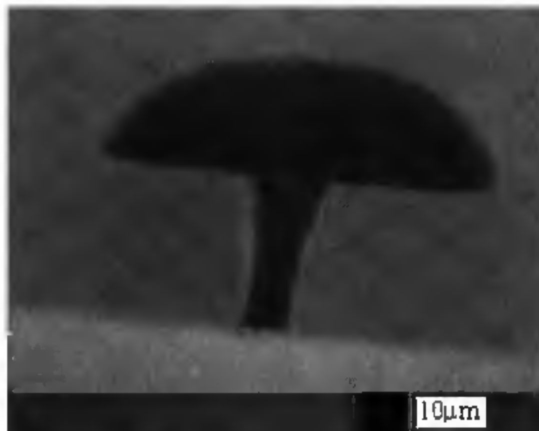

Fig. 2.16: SEM picture of nickel line with a 7 µm width (2 µm on the mask). This is the thinnest line realised with the 38 µm thick resist layer process

2.6.3. 85 µm thick resist moulds and nickel structures

The 85 µm thick resist layer photopatterning process was more delicate than the 38 µm one. The fabrication of moulds with straight edge-slope has been rendered difficult, by the fact that the resist layer was very thick. Exposure and development therefore required long periods of time.

85 µm thick resist moulds

Fig. 2.17 shows a SEM picture of an 85 µm resist structure. No division or horizontal line marks the interface between the two constitutive resist layers. The resist walls are well defined over the whole thickness. Fig. 2.18 shows a resist column structure with a square-shape base of 20 µm on a side. Due to the relatively long development time and the isotropic nature of the developer, the top of the column is circular rather than square, as originally on the mask

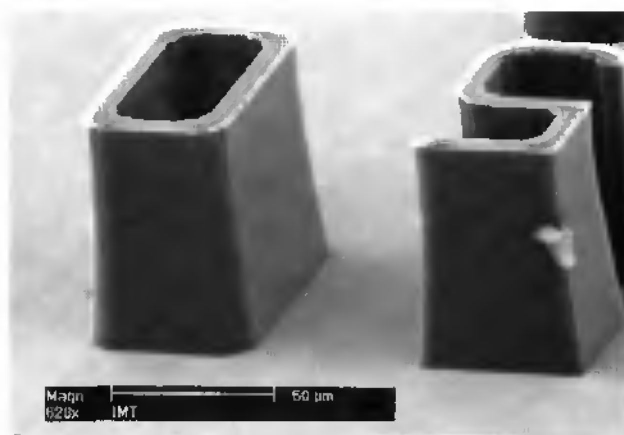

Fig. 2.17: SEM picture of an 85 µm thick resist mould. The mould is smooth over its entire height and no interface between the constitutive layers is observed.

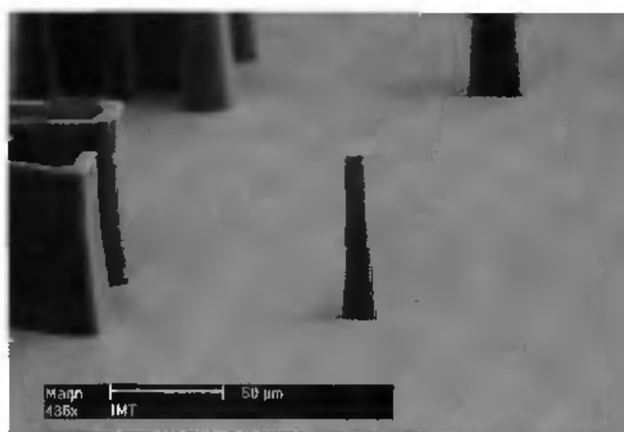

Fig. 2.18: SEM picture of an 85 µm thick resist structure. The 20 µm wide square-base shape originally on the mask has become a circular at the top.

Fig. 2.19 shows a global view of resist moulds with hollow structures of different shapes (square, circle and two differently orientated octagons). The hole dimensions are indicated by the number patterned near the structures. Holes with diameter down to 10 μm have been obtained.

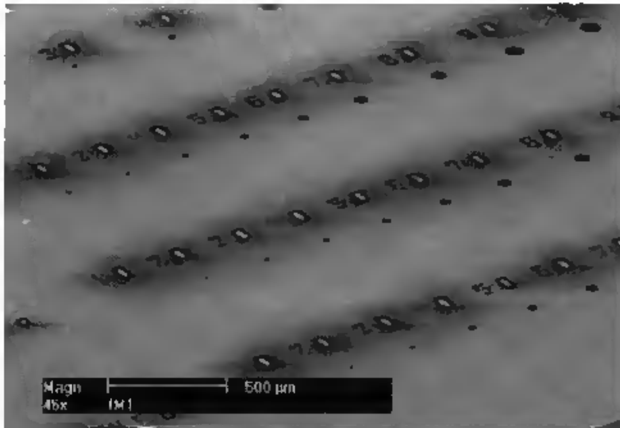

Fig. 2.19: SEM picture showing a global view of a thick resist mould for high aspect ratio Ni columns having different cross-section shapes.

Fig. 2.20 shows a SEM picture of an 85 μm thick dimension control resist structure. The determination of the enlargement has the same working principle as explained above for Fig. 2.12. The white arrow indicates the couple of structures having the same width. An enlargement of 3 to 4 μm per edge is measured.

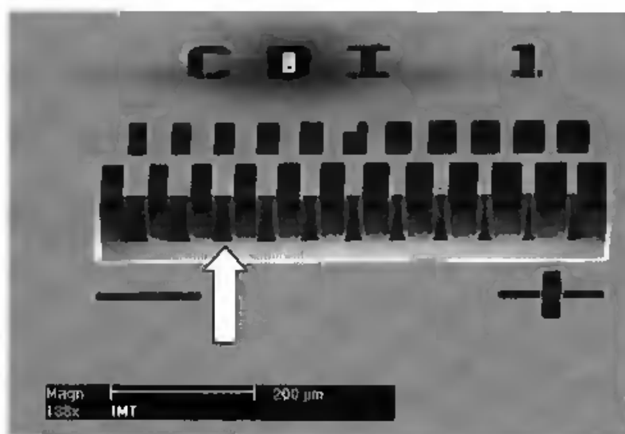

Fig. 2.20: SEM picture of an 85 µm thick dimension control resist structure. A 3 µm per edge enlargement is measured at the top of the mould.

Fig. 2.21 shows a SEM picture of a resist grid of 8 µm line width with a 16 µm pitch (on the mask).

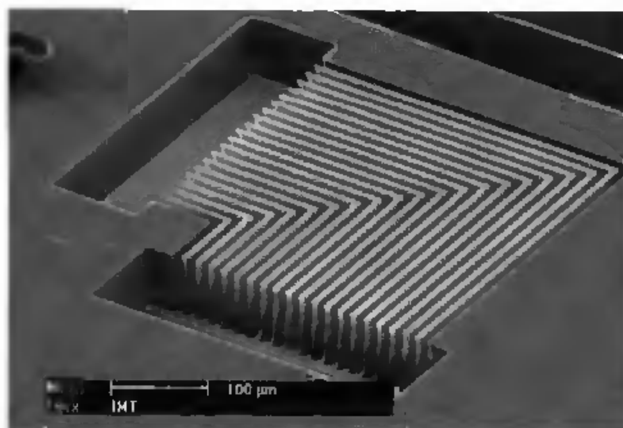

Fig. 2.21: SEM picture of an 85 µm thick line and space resist patterns. Lines width is 8 µm on the mask.

A closer view of Fig. 2.21 is given on Fig. 2.22. It shows the width limits of 85 µm high structures that can be obtained with this process. The underetching at the top of the resist layer is due to the long development time and light diffraction effects. The surface of the resist layer is not over-etched so that the dimensions of the surface mould correspond to the mask dimensions. This is due to the formation of a thin crust at the resist surface during the prebake step, which decreases its solubility in the developer.

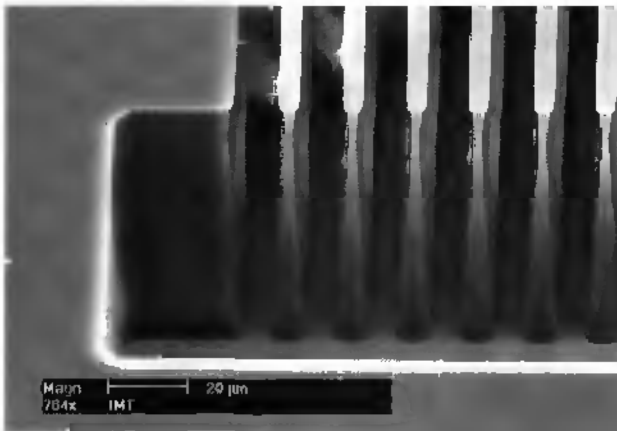

Fig. 2.22: Detail of the structure in the Fig. 2.21. The "veils" visible between the lines on the left side of the picture are SEM charging effects.

85 µm thick nickel structures

Fig. 2.23 shows a side view of an 85 µm thick T-shape nickel structure. No horizontal line at the resist layer interface is observed. Nickel overgrowth ("mushroom" like shape) delineates the height of the mould. It is observed that as for the 38 µm thick layer process, the top of the mould has been deformed due to diffraction effects [2.5]. The slope angle of the edges is about 86°.

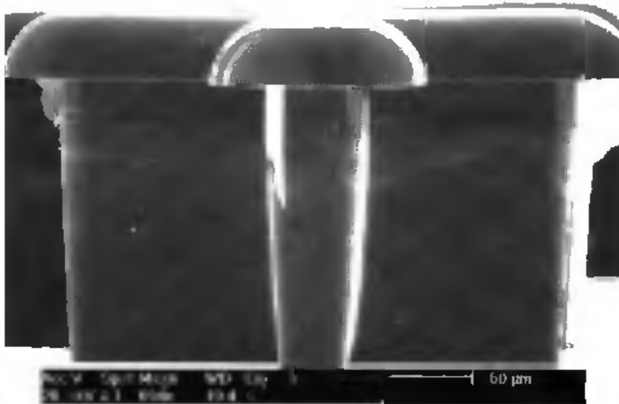

Fig. 2.23 SEM picture of 85 µm thick T-shape nickel structure.

Fig. 2.24 shows a nickel structure with a square base shape of 10 µm width on the mask, with a measured diameter of 16 µm at the bottom and 22 µm at the top of the structure. The wings located at the top of the nickel structure are due to cracks in the resist, which formed during the electrodeposition, when the process was interrupted, to measure amount of Ni deposited. The mould was taken out of the electrodeposition bath at 55 °C and the thermal shock caused cracks to appear in the resist layer. The line under the cracks indicates where the thickness measurement was done.

Fig. 2.25 shows the smallest nickel line realised with the 85 µm thick mould process. The line pattern on the mask is 1 millimetre long and 4 µm wide. The measured structure width is 10 µm at half height.

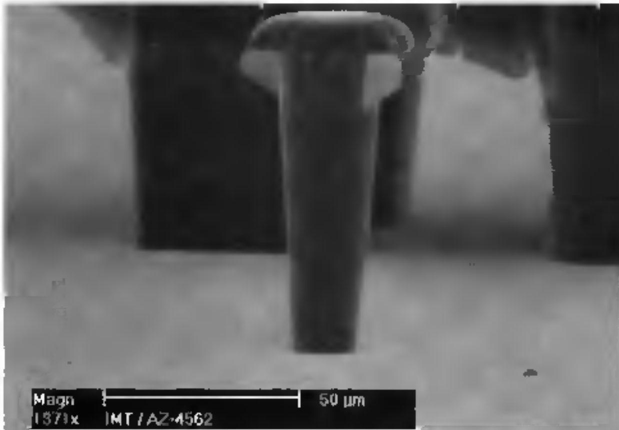

Fig. 2.24: SEM picture of square pattern on the mask with a measured diameter of 16 µm at the bottom and 22 µm at the top (10 µm on the mask).

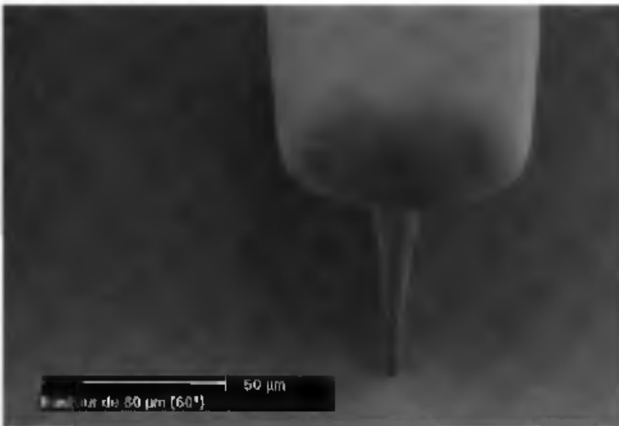

Fig. 2.25: SEM of a nickel line with a measured width of 10 µm at half-height (4 µm on the mask). This is the thinnest line realised with the 85 µm thick resist layer process.

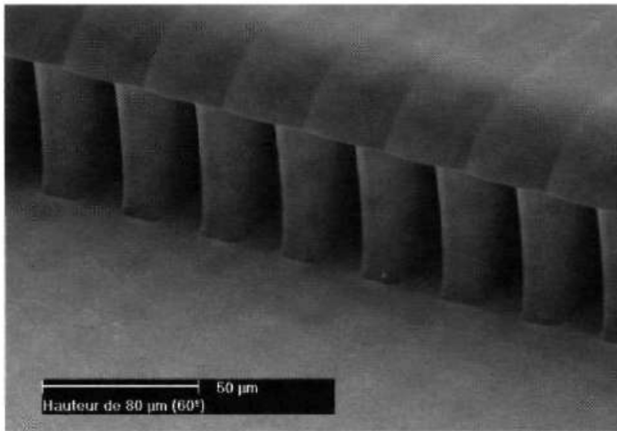

Fig. 2.26: SEM picture of a nickel grid of 15 µm wide lines and 15 µm wide spaces.

Fig. 2.26 shows a nickel grid of 15 µm wide lines and 15 µm wide spaces dimensions on the mask. The nickel electrodeposition has to be well regulated to avoid the overgrowth and to makes the final structure directly usable without any additional polishing step.

2.6.4. Discussion

The photo-patterning of thick resist layers is obviously a "capricious" technology. Each step has a non-negligible influence on the others. The results presented above show the wide range of applications of this technology. Edge-beading occurs during the coating process, and produces a layer 3 to 5 mm wide and 500-800 µm thick. The measured thicknesses are very uniform with 38 µm ± 5 % and 85 µm ± 5 %. The resist moulds are easily dissolved by acetone despite the relatively long baking processes, and no residual resist was observed on any SEM of nickel structures. No significant enlargement between the mould and the final nickel structures has been noticed.

The presented processes have some major limitations and requirements, which should be taken in account, and which are discussed below:

- The processes are reproducible as long as the temperature and the humidity of the room are stable (21°C ± 2°C and 45% ± 2 %).
- The rehydration times defined for different thicknesses should be respected. A change of the duration modifies the required exposure energy, can render the entire development of the mould difficult, and causes bubbles to be generated.
- The smallest realised lines for 38 µm process have a width of 2 µm on the mask and 7 µm on the nickel structure. For the 85 µm process, the thinnest line on the mask is 4 µm, which corresponds to a 10 µm nickel line.
- The measured enlargement between the mask and the resist patterns is 4-5 µm for the 38 µm process and 6 –8 µm for the 85 µm process.
- Because of the enlargement of the structures, compared to the mask, due to the over development of the top of the mould, thin resist walls are more difficult to obtain than thin openings.
- For both processes, the surfaces area of electrodeposition has to be well known to avoid the overgrowth of nickel. The overgrowth is particularly undesired for applications using comb like structures.

2.7. CONCLUSION

Thick resist technology has been demonstrated to be an attractive alternative to the bulk or surface micro-machining. It is fully IC compatible. The processes have been developed with conventional photolithography tools and with a commercially available photoresist. Spin coating sequences have been developed to minimise the edge-bead width and to obtain a layer thickness uniformity of 5%. A rehydration step has been introduced between the pre-bake and the exposure steps to avoid resist cracks, usually appearing during the edge bead removal, the exposure and the development steps. It has been proven that it also reduces the required exposure energy and development time, and thus the etching by the developer of the unexposed resist. A single exposure step was performed for the single and the two layers processes. It has been found that the exposure energy has to be drastically reduced and the developer concentration increased for resist layers coated on non-metallic layers. The fabricated photoresist moulds have been demonstrated to be fully compatible for nickel electroplating

It has been highlighted that to avoid nickel overgrowth, the surface area of the electrodeposition has to be carefully calculated. The overgrowth makes structures like combs or grids unusable (i.e. without an additional polishing step) and can create undesirable short-circuits between closely spaced structures. No enlargement or shape structures distortion was observed between the resist moulds and the final nickel structures.

The optimised processes have proven to be very reproducible and allow the fabrication of 38 μm, 55 μm and 85 μm thick resist moulds with a yield close to 100%. Process limitations and requirements have been determined and guide lines for the design of MEMS processes have been established.

The development of thick resist processes was realised in collaboration with L. Dellmann, as a part of his thesis work.

2.8. REFERENCES

[2.1] G. Engelmann, L. Dietrich, S. Gentzsch, R. Leutenbauer, R. Renger, H. Reichl, "Resist layer deposition and sacrificial layer technique in UV depth lithography and galvanoforming", Micro System Technologies' 96, Potsdam, 1996, pp 645-650.

[2.2] B. Loeschel, M. Rothe, S. Fehlberg, G. Gruetzner, G. Bleidiesel, " Influence of resist baking on the pattern quality of thick photoresists", Poc. of Micromachining and mirofabrication process II, Austin, USA, 1996, pp. 174-181.

[2.3] V. Conédédra, N. Fabre and M. Dilhan, " A simple optical system to optimise a high depth to width aspect ratio applied to a positive photoresist lithography process", J. Micromech: Microeng., 7, 1997, pp. 118-120.

[2.4] E. Cullmann, B. Loechel, A. Maciossek, M. Rothe, "Advanced resist processing for thick photoresist applications", Microelectronic Engineering 30, 1996, pp 551-554.

[2.5] E. Cullmann, B. Löchel and G. Engelmann, "Manufacture of 3D structures for micro systems with advanced shadow casting lithography", Micro System Technologies' 94, 1994, pp 173-182.

[2.6] E. Cullmann, "Belichtungs- und Justierungsuntersuchungen an extrem dicken Photolacken", Proceeding of VDI / VDE-IT Erzeugung dreidimensionaler Mikro-Strukturen UV-Lithographie, München, 1997

[2.7] H. Miyajima, S. Furukawa and M. Mehregany, "High aspect ratio photolithography with precise dimensional control", The Electrochemical Society Proceedings, Volume 94-32, pp 63-74, 1995.

[2.8]. M. W. Moreau, "Semiconductors lithography principles, practices, and materials", Plenum Press New York, 1988, pp. 34-38.

[2.9] H. Miyajima and M. Mehregany, "High-aspect-ratio photolithography for MEMS applications", Journal of Microelectromechanical Systems, Vol. 4, No. 4, December 1995, pp 220-229.

[2.10] M. W. Moreau, "Semiconductors lithography principles, practices, and materials", Plenum Press New York, 1988, pp. 329-333.

[2.11] Hoechst Product Information Sheet, "Standard Photoresists AZ 4500-series", 1994, p.1.

[2.12] M. W. Moreau, "Semiconductors lithography principles, practices, and materials", Plenum Press New York, 1988, pp. 488-506.

[2.13] A. Kaway, H. Nagata, H. Morimoto and M. Takata, " Local peeling of photoresist film during ultraviolet exposure", Jpn. J. Appl. Phys., Vol. 33, Part 2, No. 1B, 1994, pp. L149-L151.

[2.14] K. Suzuki, "Study on fine patterning processes with a thick resist", Sensors and Actuators A, 43, 1994, pp. 254-258.

[2.15]. I. N. Levine, "Physical Chemistry", second edition, McGraw-Hill Book company New-York, pp. 467-469, 1983.

[2.16] P.-F. Indermühle, S. Roth, L. Dellmann and N. F. de Rooij, "Patterned thick photoresist layers for protection of protruding structures during wet and dry etching processes", J. Micromech. Microeng., 8, 1998, pp. 74-76.

Chapter 3
Applications of thick photoresist patterning

3.1. INTRODUCTION

The simplicity of use of the developed thick resist process allows its combination with any standard micromachining technique, opening the way to the fabrication of new 3-dimensional micro-electromechanical systems. A number of applications are listed below.

- Microfabrication of Si cantilever and integrated tip (AFM) with a probe for the optical near field microscope (SNOM) [3.1]. The thick resist layer is used to pattern a pn-junction on the tip.

- Thick resist as protecting layer for protruding structures during wet and dry etching [3.2]; this application is presented in details in the section 3.2

- Thick resist mask used for the deep reactive ion etching process [3.3]. For example, the fabrication of Pt-tip microelectrodes for extra-cellular monitoring of activity of brain slices [3.4].

- Thick resist for transferring micro-mechanical components (tips for scanning probe microscopy) from their original to a target wafer [3.5].

- Thick resist as a mould for the electrodeposition of nickel. For example, the fabrication of a rotor for an elastic force motor, combined with SU-8 photostructuring [3.6]; the development of a clipping technology to assembly micro-fabricated structures [3.7]; the fabrication of a nickel reed relay (Chapter 4) [3.8] and the fabrication of an electrostatic gyroscope presented in details in section 3.3

3.2. PROTECTION OF PROTRUDING STRUCTURES DURING WET AND DRY ETCHING PROCESSES

3.2.1. Introduction

A simple technique is proposed here, which can be used with a standard set-up for lithography (spinner and hot plate) to protect high aspect ratio protruding structures, in this case sharp atomic force microscope (AFM) tips, in wet and dry etching.

3.2.2. Tips fabrication and thick photoresist patterning

Tips were fabricated [3.9] using an oxidised silicon wafer. Caps were patterned using standard photolithography and buffered hydrofluoric (BHF) acid. The wafer surface was then etched in potassium hydroxide (KOH), with the underetching effect being used to form the tips. As silicon etching in KOH is strongly anisotropic, the tip is formed by the intersection of crystallographic planes, and can thus be very sharp. A 4000 Å thermal silicon dioxide layer is

then grown on the wafers, to be subsequently used for wet etching experiments.

A thick positive photoresist layer (AZ-4562 / 38 µm) was spun for the lithography process with a rotating cover spinner (Karl Süss RC8 Spin Coater). The prebake was realised with a hotplate. To improve resist adhesion, a temperature ramp of 40°C to 90°C was used, after which the temperature was maintained for one hour at 90°C.

The photopatteming of the resist around the tip was realised with a mask aligner (Electronic Vision AL6-2, mercury lamp 355 nm, 405 nm and 436 nm) in proximity mode, and developed with AZ-400K [1:3] (1 part AZ-400K for 3 parts de-ionised water). A post-bake step of 15 min at 120°C is performed to stabilise the resist layer, and to avoid degassing during dry etching experiments.

3.2.3. Results

The first experiment consisted in protecting an oxidised tip with a photoresist hemisphere during a BHF etching. Fig. 3.1 shows the photoresist hemisphere after the postbake, with a diameter at its base of about 115 µm and a height of about 50 µm. The mask was a 120 µm disc and the photoresist tbickness before postbake was about 40 µm. The tip is completely covered and protected within the hemisphere.

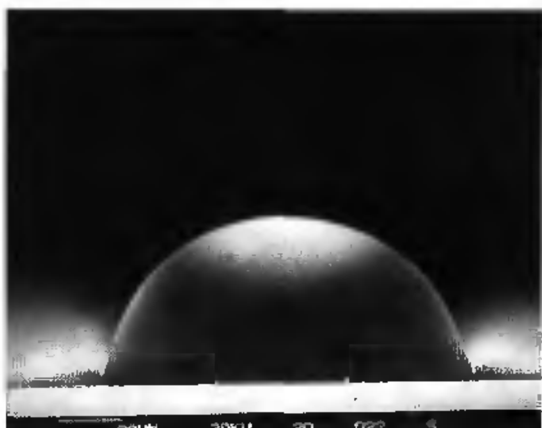

Fig. 3.1: Photoresist hemisphere after postbake (scale bar is 20 μm).

Fig. 3.2 shows an oxidised tip after oxide etching in BHF and photoresist removal. The insert in Fig. 3.2 shows a close-up view of the very top of the tip and demonstrates that it was perfectly protected during the wet etching.

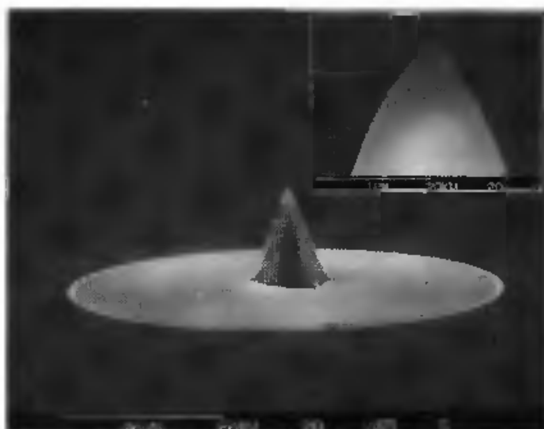

Fig. 3.2: Oxidised tip and oxide disc after BHF etching and photoresist removal. The insert shows a close up view of the top of the tip.

The second experiment consisted in defining the shape of a cantilever beam around the tip by deep reactive ion etching (DRIE). Fig. 3.3 shows a tip on a 300 μm thick cantilever beam. A close-up view (Fig. 3.4) of the very end of the tip in Fig. 3.3 shows that it was perfectly protected during the etching.

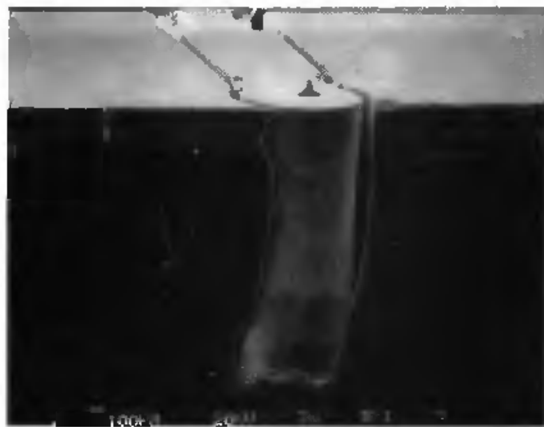

Fig. 3.3: Trenches about 300 μm deep, realised by dry etching.

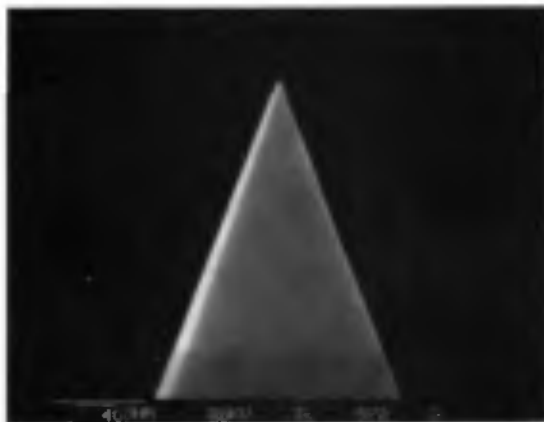

Fig. 3.4: Very top of the tip in Fig. 3.3. Estimated apex radius: less than 10 nm.

3.2.4. Conclusion

The technique presented here is convenient for the protection of protruding structures in wet and dry etching processes. As the covering photoresist layer is thick, deep dry etching can be performed to depths up to 300 µm without damaging the structures. Nevertheless, the thickness of the photoresist and its contraction during the postbake reduces drastically the lateral resolution of the lithography to about 25 µm. In spite of its low resolution, the technique which was presented above is appropriated for many micromachining applications.

The development of the process for protection of protruding structures in wet and dry etching processes was realised in collaboration with P.-F. Indermühle and L. Dellmann, as a part of their thesis works.

3.3. ELECTROSTATIC MICROFABRICATED GYROSCOPE

3.3.1. Introduction

This section is about the design and the fabrication of an electrostatic gyroscope. This application was proposed to demonstrate the thick resist mould technology suitability for MEMS fabrication. The device actuation is electrostatic and the detection capacitive.

A brief summary on the gyroscopes working principles is presented in the next paragraph. Then finite elements (FE) modal analysis simulation results are presented for different device configurations. The expected sensitivity has been calculated for one specific design. Some limitations of the thick resist moulds fabrication process and difficulties related to the sacrificial layer are discussed. Finally, some characterisation results are presented.

3.3.2. Macroscopic and micromachined gyrascopes

Usually, the word gyroscope is referring to "a rotating wheel whose axis is free to turn but maintains a fixed direction". By extension, any device, which allows to detect a change in direction, is called a gyroscope.

Macroscopic gyroscopes

Macroscopic gyroscopes can be classified in two distinct categories: optical and mechanical gyroscopes. Optical gyroscope are based on a principle called *Sagnac* effect, which was discovered at the beginning of the 20th century. The *Sagnac* effect produces, in a ring interferometer, a phase difference $\Delta\varphi$ proportional to the dot product of the rotation rate vector Ω by the area vector A enclosed by the optical path [3.10]:

$$\Delta\varphi = \frac{4\omega}{c^2}\vec{A}\cdot\vec{\Omega} \qquad \textit{Equation 3.1}$$

where ω is the angular frequency of the light source and c is the velocity of light in a vacuum.

In practice, two laser beams are moving in opposite directions in a same ring path. Any change in the direction of the system will cause a difference in the optical path length of the beams. By using interferometric measurements, very small changes are detected, so that the laser based gyroscopes are very sensitive. There are two kinds of optical gyroscopes: laser gyroscopes, which are laser with a ring cavity, and fibre gyroscopes.

Mechanical macroscopic gyroscopes consist in mechanical spinning system. The conservation of the angular momentum keeps the device pointing to the same direction.

Micromachined gyroscope

(1) Coriolis force

As free rotating structures are difficult to be microfabricated, micromachined gyroscope consist in vibrating structures. Vibrating gyroscopes make use of the fact that if a mechanical member is vibrating along one reference axis, rotation of the gyroscope frame will couple some of the vibrational energy into another axis. This coupling is due to the *Coriolis* force, an inertial force described by the French engineer-mathematician Gustave-Gaspard Coriolis in 1835. Coriolis showed that, if the ordinary Newtonian laws of motion of bodies are to be used in a rotating frame of reference, an inertial force, acting to the right of the direction of body motion for counterclockwise rotation of the reference frame or to the left for clockwise rotation, must be included in the equations of motion (Fig. 3.5) [3.11]. To simplify, if an object with a mass m is moving at velocity v in rotating frame at angular velocity Ω, a force would act on it (Equation 3.2).

$$\vec{F}_c = 2m\vec{v} \times \vec{\Omega} \qquad \textit{Equation 3.2}$$

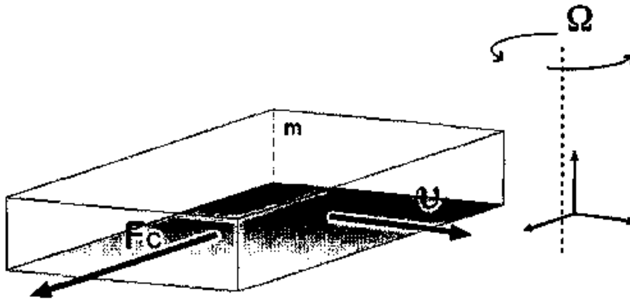

Fig. 3.5: Coriolis force mechanism.

(2) Vibrating gyroscopes

As R. Voss reported in [3.12], micromachined vibrating gyroscopes could be classified in seven different working principle: vibrating beams, tuning forks, vibrating plates, oscillating wheels, vibrating shells, dithered accelerometers and gimbals. The last few years, tuning forks, vibrating plates and vibrating shells have been the most popular presented designs.

Tuning fork and vibrating plate gyroscopes generally consist in a pair of accelerometer-like designed structures driven 180° out of phase in a direction orthogonal to their sensing axes (Fig. 3.6). The rotation induced vibration along the sensing axis could be either detected by piezoresistivity effect [3.13], capacitance variation [3.14, 3.15, 3.16] or electromagnetic effect [3.17].

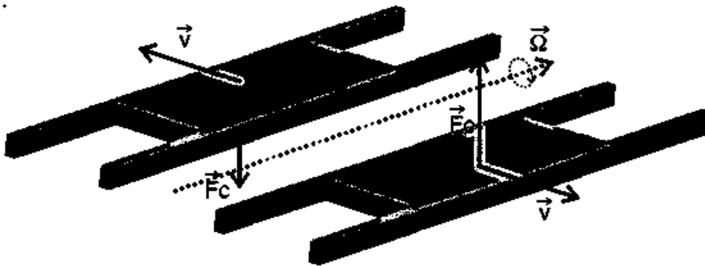

Fig. 3.6: Tuning fork gyroscope working principle

Vibrating shell or vibrating ring gyroscopes [3.18, 3.19, 3.20] are based on the principle of a ringing wineglass described by G. H. Bryan in 1890. A ring is driven into resonance in the plane of the device; and the ring's vibration forms an elliptical-shaped pattern. The four points on the ring, which have no radial deflection, are the nodes. Lines drawn through the nodes form nodial lines. The four points with maximum radial deflection (anti nodes) are located 45° away from the nodes (Fig. 3.7).

Coriolis force causes the angular position of the nodes in the elliptical vibration pattern to lag the angular position to which the sensor is rotated. During a 90° rotation, the node lines are observed to precess by about 27° [3.18]. For microfabricated ring gyroscope, the ring is vibrated into an elliptically shaped primary flexural mode with a fixed amplitude. When device is subjected to rotation, Coriolis force causes energy to be transfered from the primary mode to the secondary flexural mode, which is located 45° apart from the primary mode, causing amplitude to build up proportionally in the latter mode [3.21].

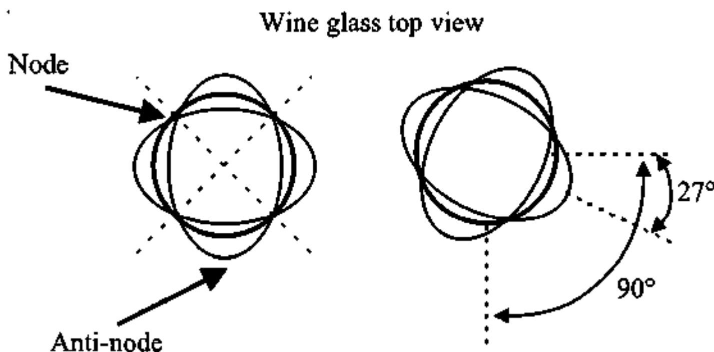

Fig. 3.7: Vibrating ring gyroscope concept illustrating by a wine glass. On the left, the initial pattern vibration and on the right the vibration pattern after 90° rotation.

3.3.3. Working principle

The proposed gyroscope is based on the tuning fork working principle. A driving electrostatic force (F_e) is generated with comb like structured electrodes [3.22](Fig. 3.8). An electrode, placed under the mass, detects capacitively the electrode/mass gap size variation induced by the Coriolis force. As the proof masses are driven 180° out of phase, the resulting Coriolis force acting on each proof mass is also 180° out of phase. The detection consists then in a differential capacitance measurement.

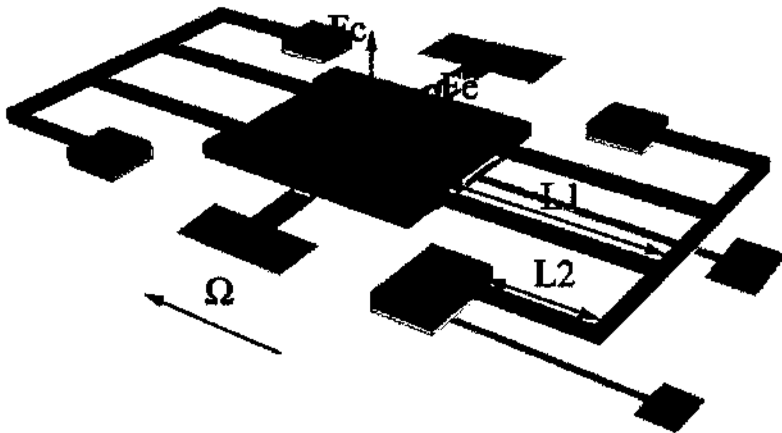

Fig. 3.8: Schematic view of the working principle of the proposed gyroscope.

3.3.4. FE modal analysis

Finite element modal analysis has been performed to define the gyroscope resonance frequencies and their corresponding mode shape. The simulations have been realised with the program *Ansys*. Geometrical parameters bave been varied to obtain a permutation of the frequency order position of the vertical (detection) and the horizontal (excitation) modes. The highest efficiency is

obtained when the sensor is designed such that the excitation and the detection modes have the same resonance frequency [3.12]. But it is extremely difficult to fabricate structures with matched eigenfrequencies. Imperfection in the fabrication leads to a mechanical coupling between the excitation and the detection oscillations. The undesired oscillation amplitude can be in the same order of magnitude as the Coriolis force and the signal may not be separated from the oscillation generated by the modes coupling [3.13, 3.23].

Modal FE analysis have been calculated for different gyroscopes, designed to have the vertical mode frequency lower, close or higher than the horizontal mode frequency. Simulations have been performed for two different mass sizes (800 x 400 μm² and 800 x 800 μm²) and for three different *L2* beam lengths (200 μm, 400 μm and 800 μm) (Fig. 3.8). *L1* beam length has been fixed at 400 μm.

Table 3.1 and Table 3.2 show the FE calculated resonance frequencies for the horizontal and vertical modes for a 800 x 400 μm² and 800 x 800 μm² proof mass respectively and for different *L2* beam lengths.

L2=	200 μm	400 μm	800 μm
Horizontal mode	6280 Hz	5820 Hz	4120 Hz
Vertical mode	9360 Hz	7740 Hz	2370 Hz

Table 3.1: Resonance frequency of the 800 x 400 μm² proof mass.

L2=	200 μm	400 μm	800 μm
Horizontal mode	4460 Hz	4140 Hz	2980 Hz
Vertical mode	6420 Hz	5350 Hz	2671 Hz

Table 3.2: Resonance frequency of the 800 x 800 μm² proof mass.

Fig. 3.9 shows the two first FE calculated mode shapes of a structure with a 800 x 400 μm^2 mass and a 400 µm long external beam (*device R1*). The model has been designed to take into account the reduction of the mass volume due to the "liberation holes" (see 3.3.5) and the structure size enlargement due to the fabrication process (see Chapter 2). The two modes showed on Fig. 3.9 correspond to the excitation (in plane) and the detection (out-plane) modes and have a resonance frequency of 5820 Hz and 7740 Hz respectively. A frequency separation of the higher resonance modes from the excitation and the detection modes has been achieved by adjusting the geometrical parameters. The next resonance mode, which also corresponds to a vertical resonance, has been shifted at 10.3 kHz.

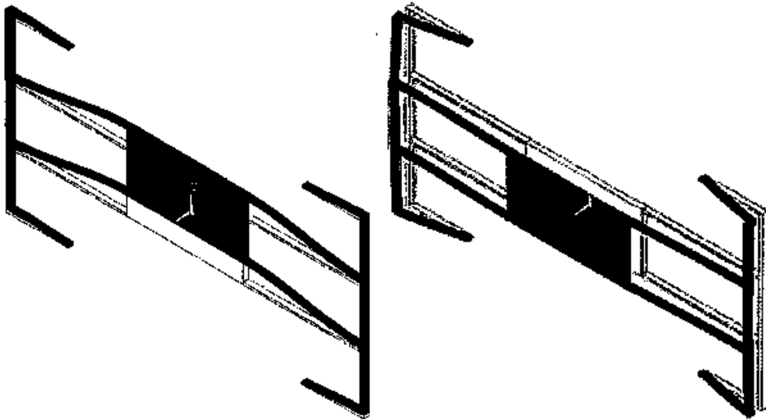

Fig. 3.9: FE modal analysis results. On the left the in-plane mode and on the right the out-plane mode.

3.3.5. Design considerations

To design the gyroscope different parameters have been considered: the FE analysis results and the known thick resist moulds fabrication process limitations.

Process limitations

(1) Comb structure

Some test structures have been designed and realised to define the adapted width of the finger and of the gap characterising the comb structure. Fig. 3.10 shows nickel electrodeposited comb test structures.

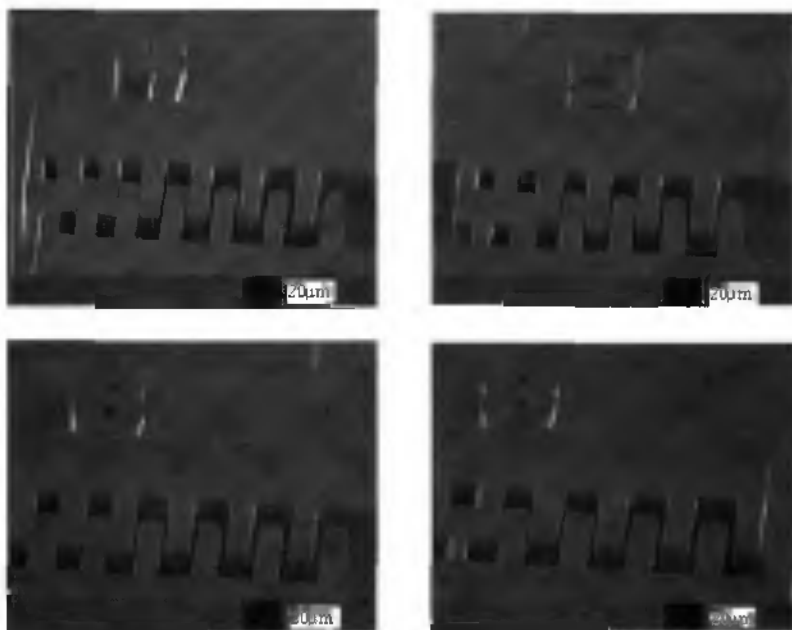

Fig. 3.10: SEM pictures of electrodeposited nickel test structures used to define the optimal parameter of a comb structure.

The gap width between the fingers is varying between 4 μm and 10 μm (on the mask). The numbers above the structures indicates the finger width. The critical parameter of comb structure is observed to be the gap width between the finger. The finger width has no influence. The minimum gap width is 6 μm on the mask. To have a good margin, the comb structure has been design to have finger of 4 μm wide and gap of 8 μm width. The total number of fingers on the proof mass is then 35.

(2) Hollow structure for the liberation of the mass

Holes have to be pierced in the proof mass to allow the penetration of the etching solution under the mass to remove the sacrificial layer. To keep a device good sensitivity, which depends on the mass value (Equation 3.2), the holes have to be as small and as few as possible. Fig. 3.11 shows an electrodeposited nickel structure with hollow prisms of different widths. The hole dimensions are indicated by the number patterned near the structures. The smallest possible prism width is 12 μm on the mask. Too small holes do not let the etching solution penetrate sufficiently under the proof mass. Finally, 16 μm wide square patterns have been included onto the proof mass pattern.

Fig. 3.11: SEM picture of a nickel structure use to determine the smallest possible hole size.

Anti-sticking structure

When large surface are separated by a small gap and are in a relatively humid environment, sticking may occur. To avoid this phenomenon, which would make a short circuit between the proof mass and the detection electrode, vertical bumpers have been included in the gyroscope design. Fig. 3.12 shows a schematic view of the bumper structure. The gap between the bumper and the substrate has been designed to be smaller than the gap between the proof mass and the detection electrode.

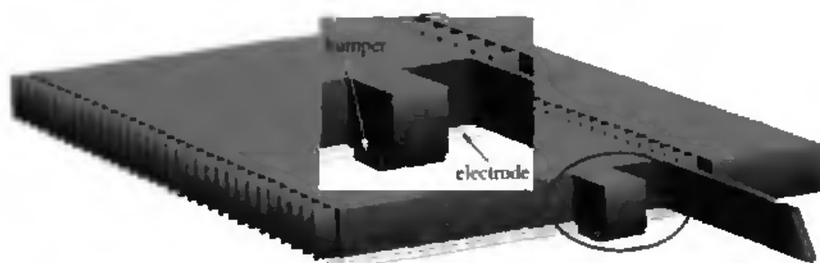

Fig. 3.12: Schematic draw of the vertical bumper used to avoid mass sticking to the electrode.

Final design

Fig. 3.13 shows the top view of the mask pattern of the nickel level. The dark grey patterns represent the structures fixed to the substrate (i.e. the anchorage, the actuation electrodes and the horizontal bumpers) and the light grey patterns represent the movable structures (i.e. the proof mass and the beams). Horizontal bumpers have been placed near the movable beam to avoid the contact of the mass with the actuation electrode, which would produce a short circuit.

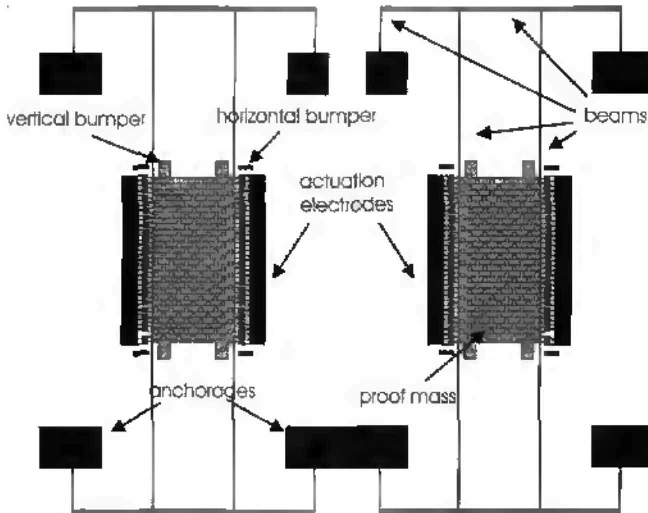

Fig. 3.13: Top view of the nickel level mask pattern. Dark grey patterns are structures fixed to the substrate and light grey patterns are movable structures.

3.3.6. Expected sensitivity

Simple analytical calculations [3.24] have been performed to estimate the sensitivity of the gyroscope.

Lateral motion

The lateral displacement Δx of the gyroscope generated by the electrical force F_e (Equation 3.3) is given by Equation 3.4.

$$F_e(t) = \frac{\varepsilon_0 n h V(t)^2}{g}$$ *Equation 3.3 [3.25]*

with: ε_0 = *air permittivity*
n = *number of finger per electrode*
h = *thickness*
V = *applied voltage between electrodes*
g = *gap width between fingers*

$$\Delta x(t) = \frac{F_e(t)}{k_x} \qquad \textit{Equation 3.4}$$

with: k_x = horizontal spring factor

The maximum velocity amplitude v_{max} is calculated with time derivation of Δx:

$$v_{\max} = 2\frac{\omega}{k_x} \cdot \frac{\varepsilon_0 nhV^2}{g} \qquad \textit{Equation 3.5}$$

with: ω = driving signal pulse

Vertical motion

The vertical motion value Δy, induced by the Coriolis force, is given by:

$$\Delta y = \frac{F_c}{k_y} \qquad \textit{Equation 3.6}$$

with: k_y = vertical spring factor
F_c = Coriolis force (Equation 3.2)

The maximum expected vertical motion is obtained by combining Equation 3.2, Equation 3.5 and Equation 3.6:

$$\Delta y_{\max} = \frac{4\omega}{k_y k_x} \cdot \rho Sh^2 \cdot \frac{\varepsilon_0 nV^2}{g} \cdot \Omega \qquad \textit{Equation 3.7}$$

with: S = proof mass surface
ν = frequency
Ω = angular velocity

The spring factor k_x and k_y could also be analytically calculated. However, they have been calculated with the existing finite element model.

Capacitance variation

The expected vertical capacitance maximal variation ΔC_{max} is then:

$$\Delta C_{\max} = \frac{S\varepsilon_0}{d^2}\Delta y_{\max}$$ *Equation 3.8*

with: S = capacitance surface
d = proof mass/detection electrode gap

Values

Table 3.3 shows the different calculated values for a gyroscope with a 400 x 800 μm² proof mass and 400 μm long *L2* beams. The process limitations have been integrated in the model (i.e. mould enlargement). The applied voltage between the electrode and the mass is 10 V and the angular velocity is 100°/s.

F_e	$5\ 10^{-07}$ [N]	F_c	10^{-10} [N]
k_x	60 [N/m]	k_y	237 [N/m]
Δx_{max}	$8\ 10^{-09}$ [m]	Δy_{max}	$4\ 10^{-13}$ [m]
v_{max}	$3\ 10^{-04}$ [m/s]	ΔC	10^{-15} [F]

Table 3.3: Different analytically calculated values.

3.3.7. Fabrication Process

A silicon dioxide layer is thermally grown and a silicon nitride layer is deposited on a substrate to improve the electrical insulation. A chromium adhesion layer and a gold seed layer are patterned by the lift-off technique (Fig. 3.14). The gold patterns define the gyro anchorages, the detection electrodes and the bonding pads.

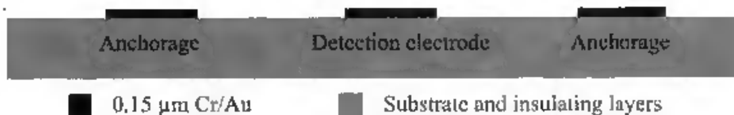

Fig. 3.14: Patterning of the gold seed layer, which defines the anchorages, detection electrodes and bonding pads.

To define the vertical bumpers, a 0.3 µm thick copper sacrificial layer is evaporated and patterned with standard photopatterned resist used as etching mask. (Fig. 3.15).

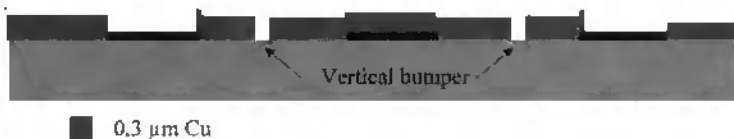

Fig. 3.15: Deposition and patterning of a 0.3 µm copper sacrificial layer which defines the vertical bumpers.

An 1 minute plasma O_2 is performed to improve the copper wet etching in a solution of sodium peroxodisulfate (8 g of $Na_2S_2O_8$ diluted in 100 g of de-ionised water). A 0.2 µm copper sacrificial layer is evaporated and patterned like the previous one (Fig. 3.16). The thickness of this layer defines the gap between the bumper and the substrate. The thickness of the two copper layers defines the gap between the gyro and the detection electrodes.

Fig. 3.16: Deposition and patterning of second copper layer.

A 55 µm thick resist layer is coated and photopatterned (see Chapter 2 for process details) and a 40 µm thick nickel layer is electrodeposited into the resist mould (Fig. 3.17).

After moulds dissolution in acetone, the sacrificial copper layers are etched in a solution of sodium peroxodisulfate (20 g of $Na_2S_2O_8$ diluted in 100 g of de-ionised water) (Fig. 3.18).

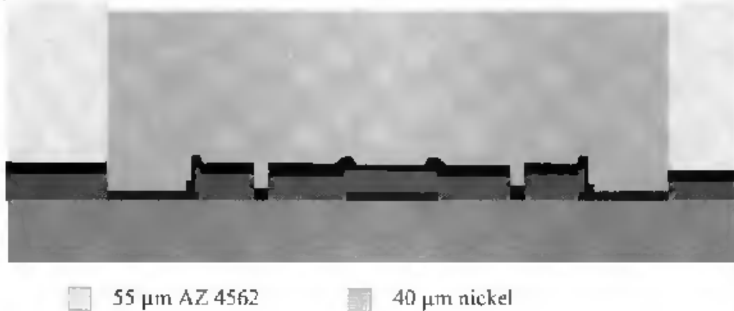

Fig. 3.17: Photopatterning of the 55 µm thick resist mould and nickel electrodeposition.

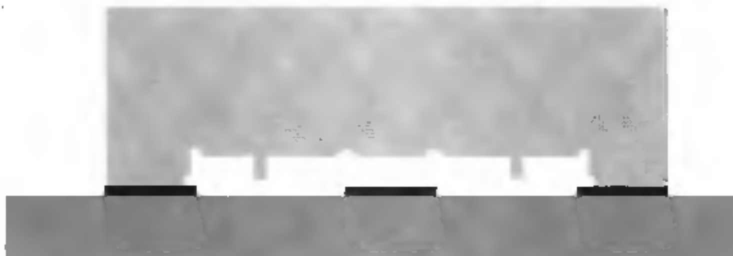

Fig. 3.18: Moulds dissolution and copper sacrificial layers etching.

3.3.8. Fabrication results

Thick photoresist moulds patterning

The gyroscope was planned to be fabricated with the 38 µm thick resist mould technology. But the difficulty to obtain nickel electrodeposition without overgrowth has motivated to develop another process technology, suitable for the fabrication of 40 µm thick nickel structures with no risk of overgrowth. The electrostatic gyroscope has been then realised with the 55 µm thick photoresist technology.

Well defined comb-like electrodes were then difficult to fabricate. As the masks were designed for the 38 µm thick resist process, the comb gap width was at the limits of the 55 µm process (minimum possible resist wall width, Fig. 3.19). But with a special care of the rehydration, exposure and development time, the fabrication of non-interconnected comb structures has been achieved.

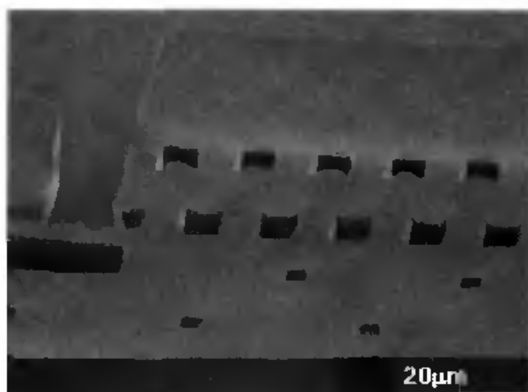

Fig. 3.19: SEM picture of an interconnected comb structure.

Sacrificial layers etching

Two metals were suitable for the sacrificial layer: titanium and copper. The copper has been preferred because of its high electrical conductivity. The adhesion of nickel is also better on copper than on titanium. To pattern the copper layers, three etching solutions were tested: a solution with iron chloride ($FeCl_3$), nitric acid and a solution with sodium peroxodisulfate. Iron chloride and nitric acid both started to etch the nickel structures after a few minutes (Fig. 3.20).

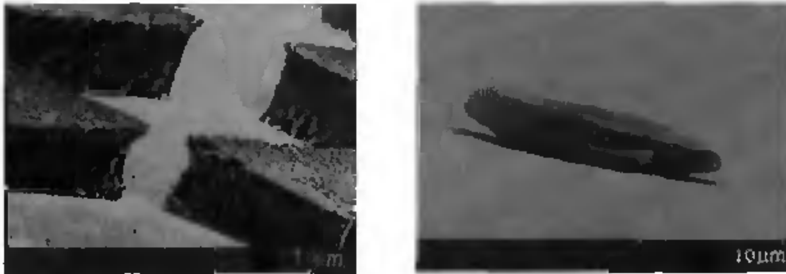

Fig. 3.20: Nickel structures after copper sacrificial layer etching in iron chloride (left) and in nitric acid (right)

The preliminary tests with the sodium peroxodisulfate etching solution showed promising results without etching the nickel structures. Nevertheless, for the long etching time required to liberate the gyroscope, nickel structures also started to be etched. The sodium peroxodisulfate solution, chemically unstable, was deteriorating in a solution, which started to etch the nickel (Fig. 3.21).

The main difficulty run up in the gyroscope fabrication was then the liberation of the device. The problem was solved by refreshing the solution and by protecting it from light, which tends to accelerate the chemical deterioration.

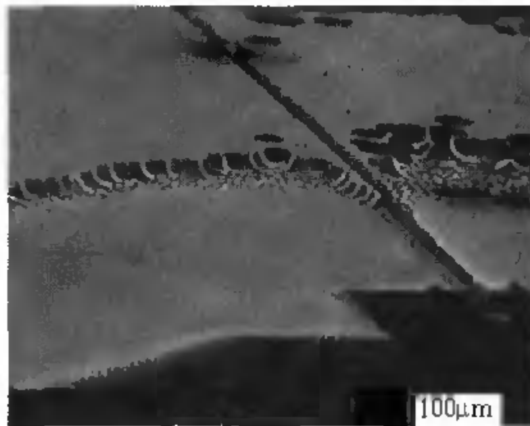

Fig. 3.21: SEM picture of electrodeposited nickel structure partially etched by the chemically deteriorated peroxodisulfate solution.

Device

Fig. 3.22 shows a SEM picture of two microfabricated nickel gyroscopes. The final chip sizes are 4 mm x 5 mm x 0.5 mm. Fig. 3.23 shows a closer view of the different part of a gyroscope: gold bonding pads, horizontal and vertical nickel bumpers, nickel anchorage and the 400 x 800 x40 μm^3 mass.

Fig. 3.24 shows a SEM picture of the comb structure, used to actuate the device, and of the square holes used to free the structure. The comb gap width is 2 µm, the finger width is 12 µm and the square hole width is 10 µm. The major difficulty was to have the complete row of non physically connected interdigitated fingers.

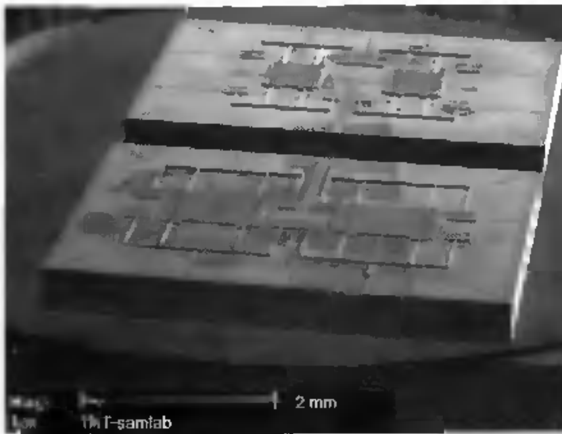

Fig. 3.22: SEM picture of two chips of microfabricated nickel gyroscopes.

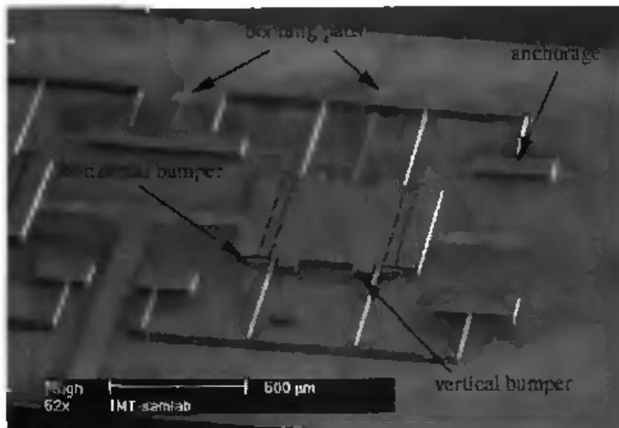

Fig. 3.23: SEM picture of an electrodeposited nickel gyroscope. The proof mass is 400 µm x 800 µm x 40µm.

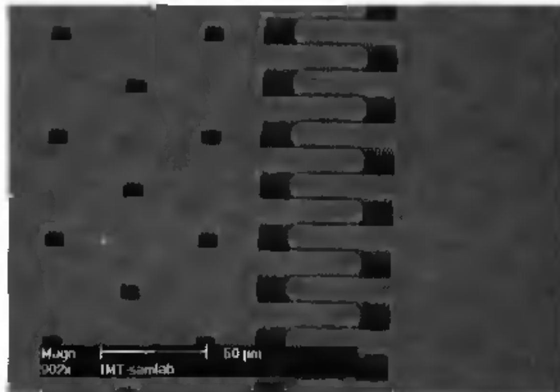

Fig. 3.24: SEM picture of the interdigitate nickel fingers. The gap width between the fingers is about 2 µm.

Fig. 3.25 shows an SEM picture of the vertical bumper region. The closest view on the upper right size of the picture shows the two different gap sizes obtained by the evaporation and the patterning of two copper sacrificial layers.

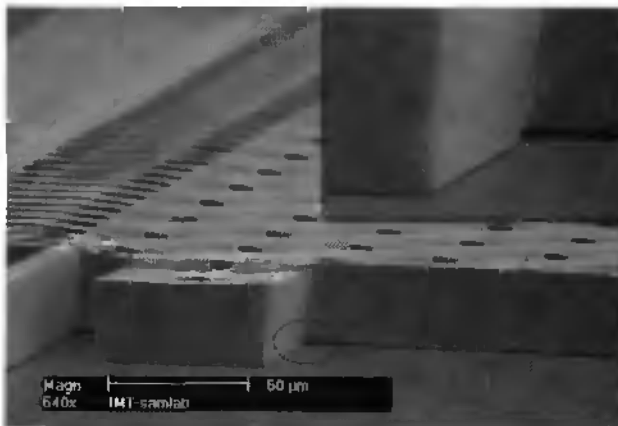

Fig. 3.25: SEM picture of a global and a detailed view of the bumper region.

3.3.9. Characterisation

Young modulus determination

To estimate the Young modulus of the electrodeposited nickel, the resonance frequency of cantilevers with different lengths have been measured. The cantilevers have been included onto the mask-set of the gyroscope and the fabrication process has then been the same. Cantilevers dimensions on the mask are 40 μm wide and are 200 μm to 1300 μm long. The measurement set-up consisted in an electrical function generator, an interferometer and a lock-in. The beam has been electrostatically actuated, through the actuation electrode, with an oscillating frequency swept signal (Fig. 3.26). The cantilever oscillation has been measured with a laser interferometer. The measured signal has been visualised and saved with the lock-in amplifier.

Fig. 3.27 shows a graph reporting the measured and the theoretically calculated [3.26] vertical beams resonance frequency versus beam length. The mean corresponding Young modulus is 212 GPa, which is close to the value of 210 GPa reported in [3.27]

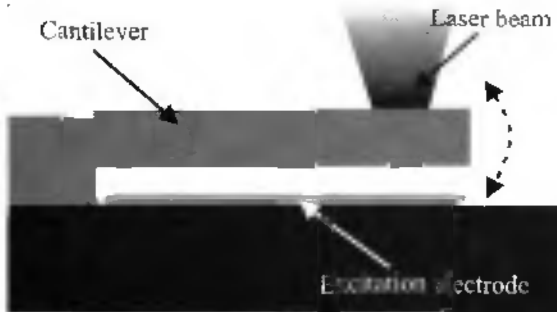

Fig. 3.26: Schematic view of the measurement principle for Young modulus estimation.

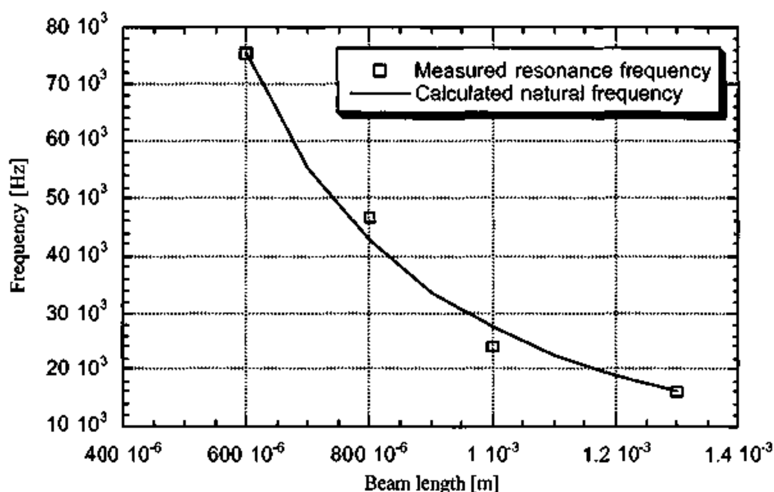

Fig. 3.27: Measured and theoretically calculated vertical resonance frequency versus beams length.

Gyroscope vertical resonance frequency

The measurement of the vertical resonance frequency was a simple test to verify that the gyroscope was moving. To overcome the difficulty of small capacitance detection, the measurement has been performed with the same measurement set-up as the previous experiment. This technique has allowed to avoid coupling effect between the actuating signal (electrical signal) and the detecting signal (optical information). The device has been vertically activated with the detection electrode and the interferometer has measured the vertical oscillation. Fig. 3.28 shows a graph representing the measured signal response for the *R1* device.

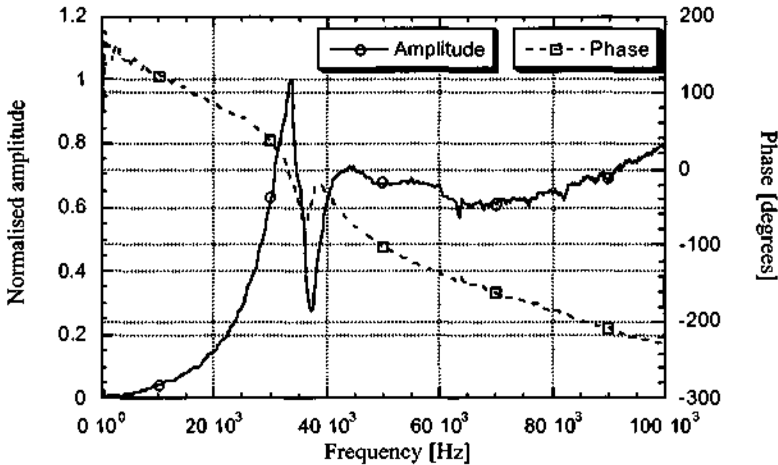

Fig. 3.28: Signal response to a vertical excitation. Two resonance frequencies are clearly observable.

A resonance and an anti-resonance modes have been detected at 34 kHz and 37 kHz respectively. Despite numerous attempts, no vertical resonance has been measured at the expected FE simulated value of 7.7 kHz (Table 3.1). The FE analysis predicts two modes at 35 kHz (9th) and at 38 kHz (10th mode) (Fig. 3.29). The 10th mode has a strong vertical oscillation component, which would correspond to the measured resonance peak. The 9th mode has no proof mass vertical oscillation component. The measured anti-resonance peak would then correspond to the 9th mode. The mode order inversion is quite acceptable. The two resonance frequencies are close and the model has not included stress or the imperfect side walls verticality of the moving beam, which could generate this small differences. The absence of the expected resonance frequency measurement is not completely understood and no satisfactory explanation has been found. However, the gyroscope is quite surely liberated; i.e. it has been manually laterally moved with a needle and a vertical motion has been measured by the interferometer, when the gyroscope has been vertically excited. The

problem seems then not to be related with the proof mass liberation or with a short circuit problem between the mass and the detection electrode, which would make impossible the actuating electrical force generation.

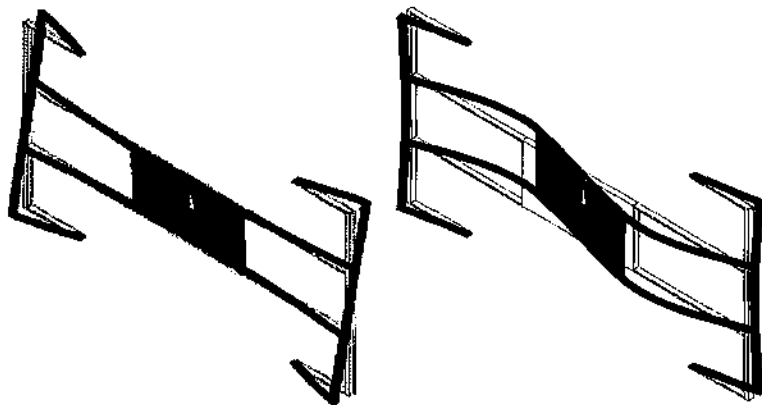

Fig. 3.29: FE calculated mode shapes of the 9th and the 10th resonance modes.

3.3.10. Conclusion

Though the few characterisation results, precious information have been obtained on the design and the fabrication of an electrostatic actuator. The thick resist mould fabrication process has shown to be appropriate for the realisation of electrostatic actuators. The main difficulties have been to fabricate non-interconnected comb fingers and to remove the copper sacrificial layer without etching the nickel structures. The first problem has been partially solved by adjusting the thick resist photopatterning parameters and would be completely cleared by redrawing the mask pattern with adequate sizes. Refreshing the etching solution before nickel started to be etched (due to a chemical degradation of the solution) has solved the second problem. Copper is then a

good candidate for sacrificial and seed layer. Mass sticking to the substrate has been successfully avoided by introducing vertical bumpers.

A study on the effects on modes coupling of the eigenfrequency relative position of the activation and the detection modes has been proposed. The corresponding geometrical parameters have been defined with finite element analysis. Unfortunately, no satisfactory measurement has been obtained to quantify the proposed experiment. The excitation and the detection modes have not been measured. Only higher resonance modes have been detected with the measurement set-up. No satisfactory explanation has been found to these observations.

Nevertheless, this work has allowed to learn more about the conception of MEMS devices. The FE analysis has shown to be a powerful tool for designing and simulating mechanical structure. Though, for simple structures, an analytical model could often be sufficient and give a good estimate of the desired parameters values. The process limitations have to be well known to be included into the model. The characterisation method should also be thought about and defined, early in the designing phase. The difficulty to measure the proof mass oscillation has been underestimated and then the measurement could not have been done completely. However, the initial planned goal has been achieved: the thick photoresist mould photopatterning technology has been demonstrated to be suitable for MEMS devices fabrication.

3.4. REFERENCES

[3.1] G. Schürmann, W. Noell, U. Staufer, N. F. de Rooij, "Microfabrication of a combined AFM-SNOM sensor, Ultramicroscopy 82, 2000, pp. 33-38.

[3.2] P.-F. Indermühle, S. Roth, L. Dellmann, and N. F. de Rooij, "Patterned thick photoresist layers for protection of protruding structures during wet and dry etching processes", J. Micromech. Microeng., 8, 1998, pp. 74-76.

[3.3] P.-A. Clerc, L. Dellmann, F. Grétillat, M.-A. Grétillat, P.-F. Indermühle, S. Jeanneret, Ph. Luginbuhl, C. Marxer, T.L. Pfeffer, G.-A. Racine, S. Roth, U. Staufer, C. Stebler, P. Thiébaud, N.F. de Rooij, "Advanced deep reactive ion etching: a versatile tool for micromechanical systems", Journal of Micromechanics and Microengineering, vol. 8, 1998, pp. 272-278.

[3.4] P. Thiébaud, C. Beuret, M. Koudelka-Hep, M. Bove, S. Martinoia, M. Grattarola, H. Jahnsen, R. Rebaudo, M. Balestrino, J. Zimmer, Y. Dupont, "An array of Pt-tip microelectrodes for extracellular monitoring of activity of brain slides", Biosensors & Bioelectronics, vol. 14, 1999, pp. 61-65.

[3.5] T. Akiyama, U. Staufer, N.F. de Rooij, "Wafer- and piece-wise Si tip transfer technologies for applications in scanning probe microscopy", IEEE Journal of Microelectromechanical Systems, vol. 8, no. 1, 1999, pp. 65-70.

[3.6] L. Dellmann, S. Roth, C. Beuret, G.-A. Racine, H. Lorenz, M. Depont, P. Renaud, P. Vettiger and N. F. de Rooij, "Fabrication process of high aspect ratio elastic and SU-8 structures for piezoelectric motor applications", Sensors and Actuators, A Physical, vol. 70, 1998, pp. 42-47.

[3.7] L. Dellmann, S. Gautsch, G.-A. Racine, N. F. de Rooij, "New integrated axle fabrication for piezoelectric motors based on a rotor clip assembling operation", Digest of Technical Papers 10th Internat. Conf. on Solid-State Sensors and Actuators, TRANSDUCERS '99, Sendai, Japan, 1999, pp. 1752-1755.

[3.8] S. Roth, C. Marxer, G. Feusier, N. F. de Rooij, "One mask nickel electroplated reed relay, Proc. MEMS'2000, Miyazaki, Japan, 2000, pp. 176-180.

[3.9] D.Wolter, Th.Bayer and J.Greschner, "Micromachined silicon sensors for scanning force microscopy", J. Vac. Sci. Technol., B 9, 1991, pp. 1353-1357.

[3.10] www.spie.org/web/oer/february/feb97/tebo.html

[3.11] Encyclopaedia Britannica, www.britanica.com, Coriolis force.

[3.12] R. Voss, "Micromachined vibrating gyroscopes", Proceedings of the SPIE 1997 Conference, Micromachined Devices and Components III, Austin, USA, 1997, pp. 62-73.

[3.13] F. Grétillat, "Silicon micromachined vibrating gyroscopes with piezoresistive detection and electromagnetic excitation", ", dissertation thesis, University of Neuchâtel, 1998.

[3.14] J. Bernstein, S. Cho, A. T. King, A. Kourepenis, P Maciel, and M. Weinberg, " A micromachined comb-drive tuning fork rate gyroscope", Proceedings of the IEEE Workshop on Micro Electro Mechanical Systems, MEMS'1993, Fort Lauderdale, USA, 1993, pp 143-148.

[3.15] J. Söderkvist, "Electrostatic excitation of tuning fork shaped angular rate sensors", Journal of Micromechanics and Microengineering, Vol 7, 1997, pp 200-203.

[3.16] K.-Y. Park, C.-W. Lee; C.-W. Lee, Y.-S. Oh, Y.-H. Cho, " Laterally oscillated and force-balanced micro vibratory rate gyroscope supported by fish-hook-shaped springs", Sensors & Actuators, A64, 1998, pp 69-76.

[3.17] S.-H. Lee, H.-T. Lim, S.-H. Kim, Y.-K. Kim, "Design of a planar vibratory gyroscope using electrostatic actuation and electromagnetic detection", Proceedings of the Symposium gyro technology, Stuttgart, Germany, 1997, pp 10.1-10.10

[3.18] M. W. Putty and K. Najafi, " A micromachined Ring Gyroscope", Technical digest of IEEE solid-state sensor and actuator workshop, Hilton Head Island, USA, 1984, pp. 213-220.

[3.19] D.R. Sparks, S.R. Zarabadi, J.D. Johnson, Q. Jiang, M. Chia, O. Larsen, W. Higdon, P. Castillo-Borelley, " A CMOS integrated surface micromachined angular rate sensor: it's automotive application", Digest of Technical Papers 9th Internat. Conf. on Solid-State Sensors and Actuators, TRANSDUCERS '97, Chicago, USA, 1997, pp. 851-854.

[3.20] C. Fell, I. Hopkin, K. Townsend, I. Sturland, "A second generation silicon ring gyroscope", Symposium Gyro Technology, Stuttgart, Germany, 1999, pp 1.1 - 1.14.

[3.21] F. Ayzi and K. Najafi, "Design and fabrication of a high-performance polysilicon vibrating ring gyroscope", Proceedings of the 11th IEEE Workshop on Micro Electro Mechanical Systems, MEMS'1998, Heidelberg, Germany, 1998, pp 621-626.

[3.22] R. Legtenberg, A. W. Groeneveld and M. Elwenspoek, "Comb-drive actuators for large displacements", Journal of Micromechanics and Microengineering, Vol 6, No 3, 1996, pp 320-329.

[3.23] W. Geiger, B. Folkmer, J. Merz, H. Sandmaier, W. Lang, " A new silicon rate gyroscope", Proceedings of the 11th IEEE Workshop on Micro Electro Mechanical Systems, MEMS'1998, Heidelberg, Germany, 1998, pp 615-620.

[3.24] Y. Mochida, M. Tamura, K. Ohwada, " A micromachined vibrating gyroscope with independent beams for the drive and the detection mode", Sensors & Actuators, A80, 2000, pp. 170-178.

[3.25] V. P. Jaecklin, "Surface micromachined electrostatic actuators", dissertation thesis, University of Neuchâtel, 1994, pp 15-17.

[3.26] W. C. Young, "Roark's formulas for stress and strain", 6th ed, McGraw-Hill international editions, 1989, *equ. 3b*, pp 714

[3.27] Commissions romandes de mathématiques, de physiques et de chimie, « Formulaires et tables », éditions du Tricorne, 1985, pp 194

Chapter 4
Microfabricated Reed Relay

4.1. INTRODUCTION

Macroscopic relays are broadly applied in electronic switching where high resistance and low capacitance isolation is necessary, and where low on-resistance is advantageous, such as in precision electronic instruments. No solid-state switch (e. g. CMOS transmission gate, JFET, etc.) has yet demonstrated the outstanding off-state isolation, low crosstalk, and on-resistance of conventional, electromagnetic relays. However, a growing number of efforts are being made to micromachine mechanical relays for inclusion on IC substrates. These last few years, several micro-machined relays have been presented that use electrostatic [4.1, 4.2, 4.3, 4.4], thermal [4.2, 4.5], magnetostatic [4.6] and electromagnetic [4.7] actuation. All are based on the same switching principle: a movable structure is physically in contact or separated by an insulating gap (gas or vacuum).

Some of the working principles or designs proposed these last few years for electromagnetic actuators or devices are also applicable for electromagnetic microrelay applications. Different approaches to fabricate or to integrate electromagnet have been proposed:

- devices with standard (non microfabricated) electromagnet and without core connection with the microfabricated structure [4.8]
- devices with partially microfabricated coil and with a core connection with the microfabricated structure [4.9, 4.10]
- microfabricated electromagnet [4.11, 4.12, 4.13]
- devices which integrated microfabricated electromagnets [4.14, 4.15, 4.16, 4.17, 4.18, 4.7].

The use of integrated microfabricated coils requires complex fabrication processes while providing a limited number of turn in the electromagnet's coil.

This chapter describes the design, the fabrication and the characterisation of a microfabricated reed relay, suitable for position detection applications, by detecting the presence of an external magnetic field. The proposed device includes also a self-test function, which can be activated without approaching the relay. The magnetic field is supplied by an external magnet (or electromagnet) for the detection mode and by a hybrid mounted coil for the self-test mode. The total packaged device dimensions are 5x5x1 mm^3. To realise the device, nickel material has been chosen because of its good magnetic properties and its ability to be electrodeposited. The fabrication process requires a single photolithography step. The relay has been fabricated using the 55 μm thick positive resist photopatterning process described in Chapter 2. Electrical, magnetic, static and dynamic characterisations have been performed. A theoretical model of the switch is also proposed and compared with the obtained measurements. Some microrelays have also been fabricated with electrodeposited iron-nickel.

4.2. DESIGN

4.2.1. Working principle

Based on the reed relay working principle, the micro-relay consists of a *beam* moving laterally to contact a *contact pad.* The actuation force is generated by an external magnetic field supplied either by an external permanent magnet or electromagnet. To guide the magnetic field and to insure the generation of a sufficiently large magnetic force to actuate the beam, *profiled structures* have been integrated in the design (Fig. 4.1). The *electrical ports* have been separated by an air gap from the profiled structures to avoid current leakage. To simplify the fabrication process and to insure a high enough ampere-turn number, it was decided not to microfabricate the self-test function coil. The packaged device consists then of four electrical ports: the input port, the output port and two ports for the self-test coil.

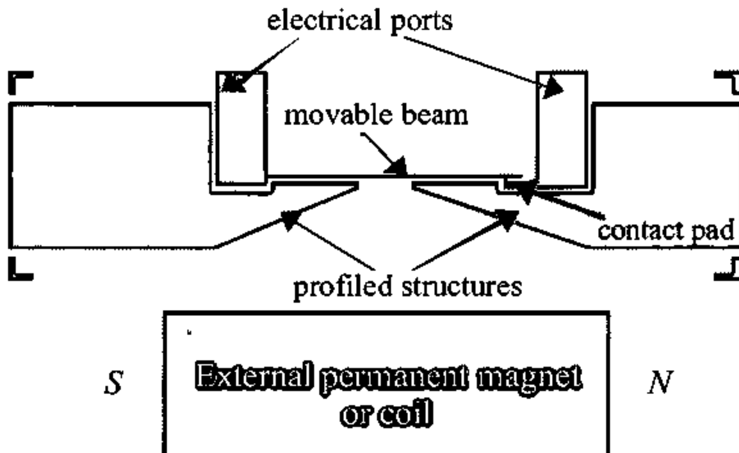

Fig. 4.1: Schematic top view of the microfabricated reed relay. An external permanent magnet or coil supplies the required magnetic field to close the switch.

4.2.2. Design considerations

To insure the device a good sensitivity, different parameters, such as the beam lateral spring constant and the contact pad/beam gap width, have been considered. The beam lateral spring constant mainly depends on length and width (see § 4.4, Equation 4.7). The mechanical force required to close the relay is dependent on the beam spring constant and on the contact pad/beam gap width. To minimise the magnetic field needed to close the relay, the best switch design should have the smallest possible contact pad/beam gap width and the largest possible length/width ratio.

Considering the limitations induced by the 55 μm thick resist photo-patterning process (see § 4.3.2), relays having a 8 μm wide beam with a length of 1000 μm, 1500 μm or 2000 μm and a 10 μm contact pad/beam gap width have been designed. A relay with a special contact pad geometry used to reduce the lateral sticking and with a 1000 μm long and a 8 μm wide beam has also been designed (Fig. 4.2). The switch and the coil have been planed to be mounted into 5 x 5 mm^2 *Surface Mounted Device* (SMD) package and the chips have been designed to have the final dimensions of 1 mm in width and 3 mm in length.

Fig. 4.2 Schematic top view of the contact pads: on the left the standard geometry and on the right the special geometry for sticking minimisation.

4.3. FABRICATION

4.3.1. Fabrication process

The fabrication process requires single photolithography step. To improve the electrical insulation, a silicon dioxide layer (2000 Å) is thermally grown and a silicon nitride layer (2000 Å) is deposited on a 4 inches silicon wafer. To increase the gap size between the movable beam and the substrate, a 1 μm thick n-type doped silicon dioxide sacrificial layer is deposited on the nitride layer. A 0.02 μm thick titanium adhesion layer and a 1 μm thick copper seed and sacrificial layer are finally evaporated (Fig. 4.3a). Different reasons have motivated the use of copper as sacrificial layer material: it has a low electrical resistivity, it can be selectively etched and nickel has a good adhesion on it.

To improve the adhesion of the photoresist on the substrate, a dehydration step is performed. The substrate is diped in an isopropanol solution for ten minutes and then dried in a ventilated oven at 60° C. The standard process consisting in a 30 minutes long dehydration in a oven at 200° C cannot be applied in this case because of the copper oxidation risk. A 55 μm thick resist layer is then coated, baked and photo-patterned (see Chapter 2, § 2.3 to 2.5 for process details). No post-bake is performed after development to avoid deformation of the moulds [4.19]. Nickel is then electro-deposited from a commercial bath (Fig. 4.3b). After the completed growth of the nickel layer (40 μm), the photoresist moulds are dissolved in acetone. The sacrificial layers are then partially etched. The etching time has to be long enough to free the movable beam and sufficiently short to keep the other nickel structures fixed. The copper layer is etched in a solution of sodium peroxodisulfate (25g of $Na_2S_2O_8$ diluted in 125g of de-ionised water) for four minutes. The titanium and the n-type-doped silicon dioxide layers are partially etched in buffered hydrofluoric acid (BHF) for three minutes (Fig. 4.3c).

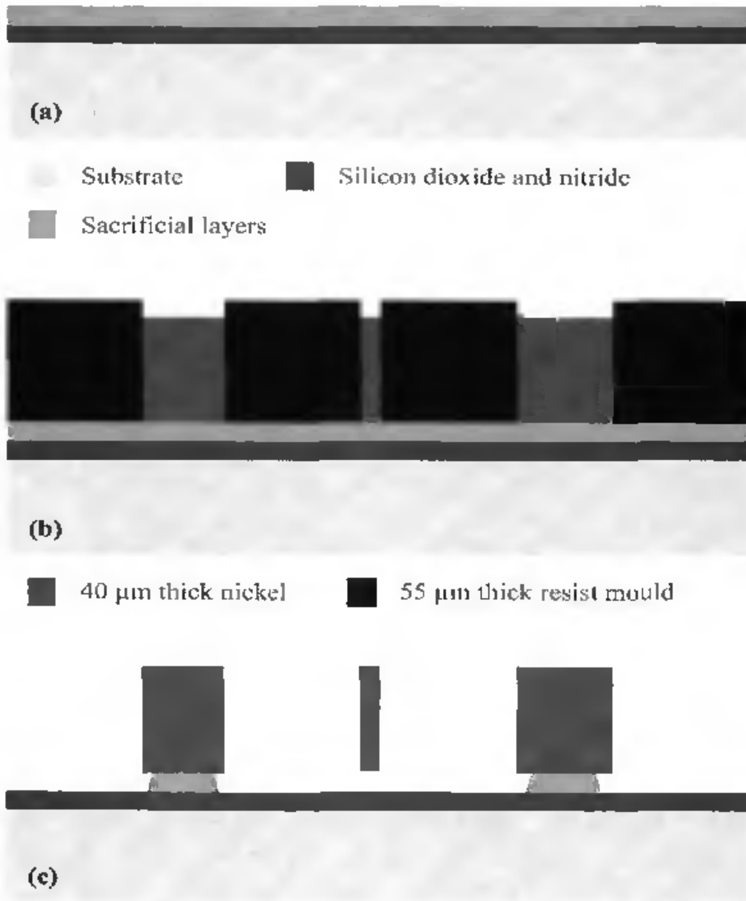

Fig. 4.3: Schematic view of the relay fabrication process. ***(a)*** *Deposition of a silicon dioxide and a silicon nitride insulation layers. Deposition of a doped silicon dioxide and a Ti/Cu sacrificial layers.* ***(b)*** *Coating, baking and photopatterning of the 55 µm thick resist moulds. Electrodeposition of the 40 µm thick nickel layer.* ***(c)*** *Dissolution of the moulds and partial etching of the sacrificial layers.*

For some devices, an electroless deposition of a 700 Å thick gold layer or an evaporation of a 500 Å thick silver layer is performed to improve the electrical contact resistance. The electroless deposition of gold on nickel is performed from a commercial agitated bath (Heraskin 7205) at 45° C for two minutes.

The last steps of tbe process consist in wafer dicing, packaging and wire bonding of the chips. To avoid the deformation of the movable beam during the dicing process, an 85 μm thick resist protective layer is coated on the whole substrate. The coating process (see Chapter 2, § 2.3) is well suited for this application as it doesn't involved any high spinning speed. After the dicing, the photoresist is stripped in acetone and in isopropanol. To prevent the beam sticking on the contact pad and to reduce the risk of beam plastic deformation due to nitrogen blow-gun relatively high pressure flux, the drying of the diced chips is performed in a vacuum oven at 60° C.

4.3.2. Process limitations

Some general process limitations (e.g. side walls, layer uniformity) have already been reported in the Chapter 2. In this paragraph, process limitations, related to the switch application, are reported. Different test structures have been included onto the fabrication mask to define guide lines for the 55 μm thick resist layer process and for the design of future switches generation.

Pattern enlargement

The enlargement between the resist and the mask patterns has been determined with the same test structure, which bas been described in Chapter 2. On Fig. 4.4 an enlargement of 2.5 μm per edge is observed.

Fig. 4.4: SEM picture of a 55 µm thick dimension control resist structure. A 2.5 µm per edge enlargement is measured at the top of the mould.

Minimal resist width

One critical parameter of the thick resist mould technology is the minimum resist wall width. It is a particularly sensitive parameter for the design of the switch because it defines the smallest gap between the movable beam, the "profiled structures" and the contact pad. The dissolution rate by the developer of the unexposed resist regions is slower, but not null, compared to the exposed regions. For thick resist layers, the development time is long enough to start the etching of the unexposed resist region. For narrow resist structure, the consequence is, after metal electrodeposition, an undesired structures interconnection. The test structure shown on Fig. 4.5 has been designed to determine the thinnest possible resist wall. In order to separate each parameter influence from the others, the resist walls have the same length (1 mm and 20 µm), are spaced 20 µm from each other and have a width of 4 µm to 10 µm (with 1 µm increment), 15 µm and 20 µm.

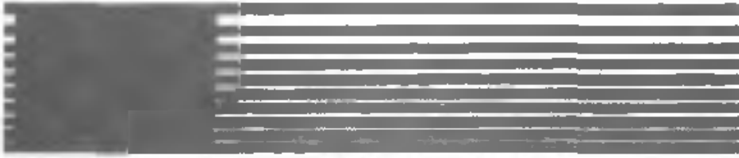

Fig. 4.5: Schematic top view of a test structure, which is used to determine the minimum possible resist wall width. The white colour represents the photoresist.

The SEM pictures on Fig. 4.6 and Fig. 4.7 show the fabricated resist test structures. The developer has etched the 4 to 6 µm wide resist walls. The 7 µm wide resist top wall has been etched. The 8 µm wide resist wall (white arrows) is then the thinnest resist wall. Wall length has no significant effect on the minimum realisable wall width. However, at the right end of the resist walls on Fig. 4.7, a lateral etching is observed.

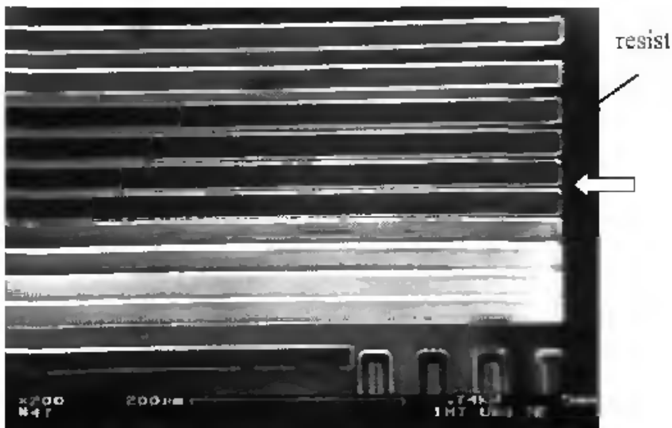

Fig. 4.6: SEM picture of the 55 µm thick resist test structure used to determine the minimum resist width. The thinnest realisable resist wall, indicated by the white arrow, is 8 µm wide on the mask.

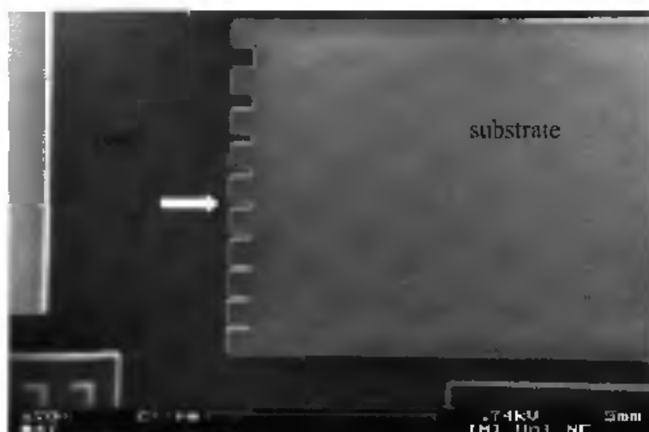

Fig. 4.7: SEM picture of the 55 µm thick resist test structure used to determine the minimum resist width.

Minimal resist length

Another interesting parameter to determine is the shortest realisable resist wall length for a fixed width. For the switch design this parameter is particularly important because it determines the minimum gap length between the movable beam and the contact pad. The test structure shown on Fig. 4.8 was designed to determine the minimal possible resist wall length. As for the previous test structure, only one parameter is varying. The resist walls have a fixed width of 10 µm, are spaced 20 µm from each other and have a length of 4 µm to 10 µm (with 1 µm increment), 15 µm and 20 µm.

Fig. 4.8: Schematic top view of a test structure, which is used to determine the minimal possible resist wall length. The white colour represents the photoresist.

Fig. 4.9: SEM picture of the 55 μm thick resist test structure used to determine the minimum resist length. The length limit is located between 10 and 15 μm (white arrow).

The SEM picture on Fig. 4.9 shows the fabricated resist test structure. The determination of the minimal resist wall length is relatively subjective. The 4-10 μm long resist structures have rounded corners. The minimum wall length is located between 10 μm and 15 μm (white arrow).

Resist corner shape

The last test structure shown on Fig. 4.10 was designed to determine the minimum path width for a corner shape. For the switch design, this parameter is particularly important because it determines the minimum corner path width of the gap located between the contact pad and the profiled structure, and between the movable beam and the contact pad.

As for the previous test structures, only one parameter is varying. The resist corners occupy a fixed area of 20 μm by 20 μm, are spaced 20 μm from each other and have a path width of 5 μm to 10 μm (with 1 μm increment), 15 μm and 20 μm.

Fig. 4.10: Schematic view of a test structure, which is used to determine the thinnest possible resist corner shape. The white colour represents the photoresist.

Fig. 4.11 shows a SEM picture of the resist test structures. The first three structures are etched at their top height. The 8 µm wide path corner structure is then the first one which is not etched. The concave angle is observed to be more rounded than the convex one, which is a characteristic of isotropic etchings.

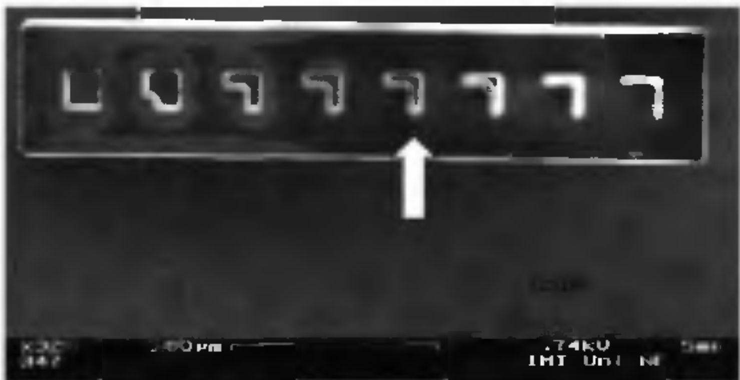

Fig. 4.11: SEM picture of the 55 µm thick resist test structure used to determine the minimum resist path width for a corner shape. The minimal corner path width is 8 µm (white arrow).

4.3.3. Fabrication results

The Fig. 4.12 shows a SEM picture of the microfabricated reed relay after the dicing step. The chip is 3 millimetres long, 1 millimetre wide and 400 micrometers thick.

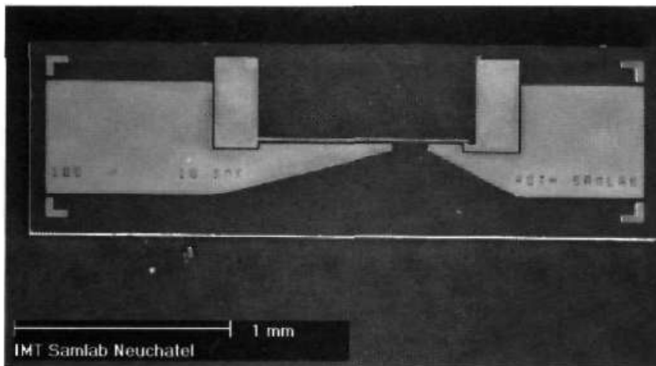

Fig. 4.12: SEM picture of the microfabricated nickel reed relay after dicing. Chip dimensions are 1 x 3 x 0.4 mm³.

The close view of the contact pad/beam region (Fig. 4.13) shows that the slope of the moulds is not perfectly vertical. Due to the pattern enlargement, contact pad/beam gap width has been reduced to approximately 4 µm and the movable beam is 1 mm long, 14 µm wide and 40 µm thick.

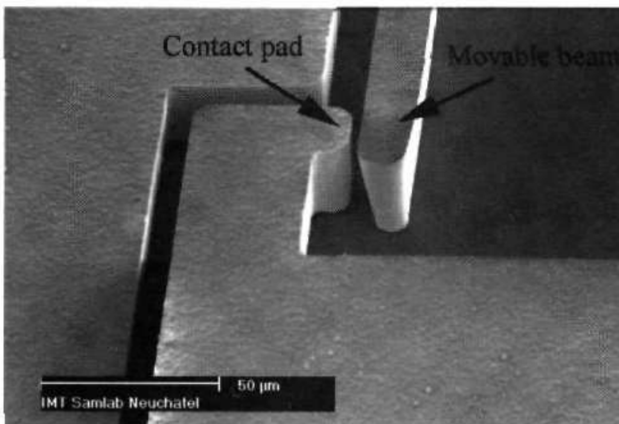

Fig. 4.13: SEM picture of the contact pad/beam region. Gap width is approximately 4 µm. The movable beam is 1 mm long, 14 µm wide and 40 µm thick.

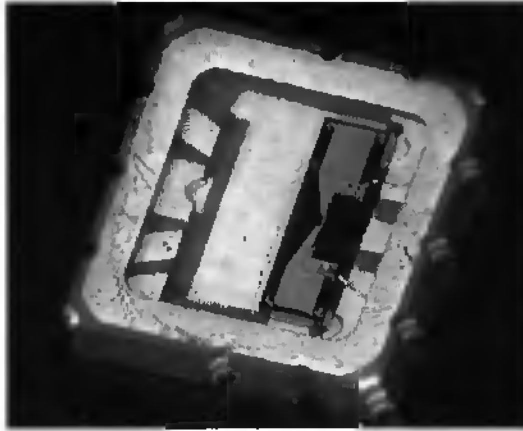

Fig. 4.14: Photograph of the microfabricated nickel relay mounted and wire-bonded on the SMD support.

The top surface of the nickel structures is observed to be smooth, which has allowed the wire bonding directly on the nickel electrical ports (Fig. 4.14).

4.4. ANALYTICAL MODEL CALCULATION

The magnetic field required to close the switch has been estimated with a simple analytical calculation. It has allowed to determine which parameters were critical for the switch design. Some hypotheses have been done to simplify the calculation of the required permanent magnet field intensity and the coil ampere-turns value. It has been assumed that:

- the magnetic force is applied at one point located at the free end of the movable beam.
- the magnetic force is time constant.
- there are no magnetic flux loss between the different part of the switch components.

- the magnetic field located in the gap (between the movable beam and the profiled structures) has only one lateral component perpendicular to the beam.
- the magnetic field is small enough to consider the different material permeability to be a constant.
- the magnetic field lines are defined by a mean path and are assumed to follow the shape of the geometry (i. e. corners...)[4.20].
- the induction is uniformly distributed on the perpendicular cross sectional area [4.20].

The calculation method has been separated in three different parts:

- Definition, description and calculation of the equivalent magnetic reluctance circuit model.
- Determination of the force required to close the switch and of the corresponding required magnetic induction.
- Calculation of the required ampere-turn value for the self-test coil.

4.4.1. Magnetic reluctance

The calculation of the required magnetic field to close the switch, generated by an external magnet or coil, is obtained by representing the device with an equivalent magnetic circuit. By analogy with electrical circuits, an Ohm-like law for magnetism (Equation 4.1) is used. The magnetic flux Φ (Equation 4.2) corresponds to the electrical current, the magnetic potential Θ_{ab} (Equation 4.3)

to the electrical potential and the magnetic reluctance R_t (Equation 4.4) to the electrical resistance.

$$\Theta_{ab} = R_t \cdot \Phi$$ *Equation 4.1*

$$\Phi = B \cdot S$$ *Equation 4.2*

with: *B= magnetic induction*
S= cross sectional area

$$\Theta_{ab} = H \cdot l_{ab}$$ *Equation 4.3*

with: *H= magnetic field*
l_{ab} *= magnetic path between a & b.*

$$R_t = \frac{l_t}{\mu_t \cdot A_t}$$ *Equation 4.4*

with: l_t *= magnetic field lines path length*
A_t *= cross sectional area*
μ_t *= magnetic permeability of the material*

4.4.2. Magnetic reluctance equivalent circuit

The switch has to be first schematically decomposed in different reluctance parts (Fig. 4.15) and the total equivalent magnetic reluctance then calculated. The reluctances labelled with the letter "*a*" correspond to the air gaps. R_1 to R_6 represent the profiled structures and the left electrical port. R_b represents the movable beam. R_7 and R_8 the right electrical port and the contact pad. Ra_1 and Ra_8 represent the air gap between the coil or the magnet and the switch. The total equivalent reluctance calculation of serial or parallel reluctances is the same as for electrical resistances. The equivalent reluctance of serial reluctances is the addition of all serial reluctances. The equivalent reluctance of parallel reluctances is equal to the inverse value of the addition of the inverse value of each parallel reluctance.

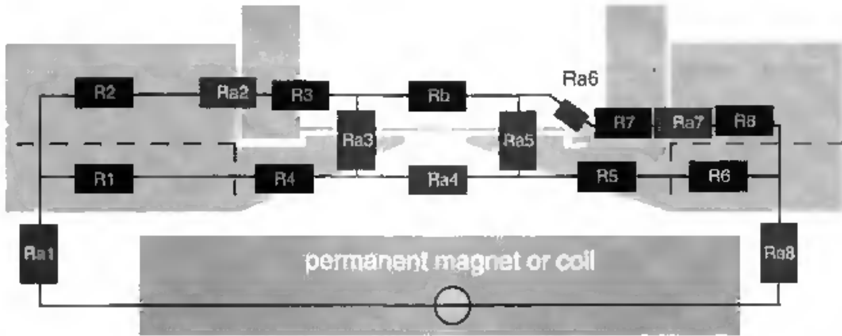

Fig. 4.15: Schematic view of the switch decomposed in different reluctances.

Some observations allow the simplification of the model:

- the contact pad and the right electrical port are connected in serial with two air gap. It results in a high equivalent reluctance, which is connected in parallel to the rest of the circuit. The reluctance R7, R8, Ra6 and Ra7 can be therefore neglected.

- the air gap between the profiled structures has a very high reluctance value. Ra_4 can be therefore neglected.

Fig. 4.16 shows the simplified reluctance circuit.

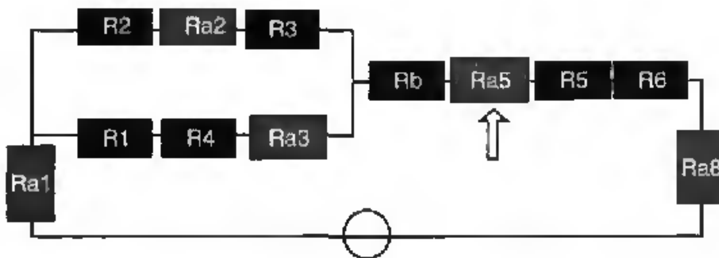

Fig. 4.16: Simplified magnetic reluctances circuit.

The total switch (with the outside air gaps) reluctance value is then equal to:

$$R_{tot} = \frac{R_m \cdot R_n}{R_m + R_n} + R_p + Ra_1 + Ra_8 \qquad \textit{Equation 4.5}$$

with: $R_m = R_2 + Ra_2 + R_3$

$R_n = R_1 + R_4 + Ra_3$

$R_p = R_b + Ra_5 + R_5 + R_6$

The required magnetic potential to close the switch is then expressed by:

$$\Theta_{ab} = R_{tot} \cdot \Phi \qquad \textit{Equation 4.6}$$

Next step is the determination of required the magnetic flux Φ in Ra_5 and the corresponding magnetic force to close the switch.

4.4.3. Required magnetic force and flux

To determine the magnetic force, the required mechanical force has to be first calculated. The Fig. 4.17 shows a schematic close view of the contact pad/beam region, together with the relevant parameters.

The lateral spring constant k_x of the movable beam is expressed by [4.21]:

$$k_x = \frac{E \cdot t_b \cdot w_b{}^3}{4 \cdot l_b{}^3} \qquad \textit{Equation 4.7}$$

with: E = *Young modulus* $[Nm^{-2}]$

t_b = *beam thickness [m]*

w_b = *beam width [m]*

l_b = *beam length [m]*

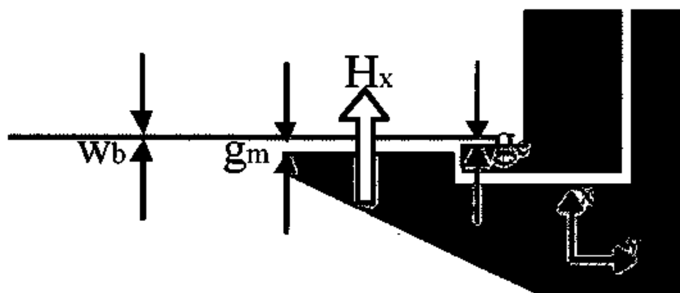

Fig. 4.17: Schematic close view of the beam, the profiled structure and the contact pad area.

The required mechanical force F_k to move the beam for a distance g_e is then equal to:

$$F_k = k_x \cdot g_e \qquad \text{Equation 4.8}$$

with g_e = *the gap between the movable beam and the contact pad [m]*

The expression of the lateral magnetic force generated by the magnetic field $\boldsymbol{H_x}$ is given in Equation 4.9 [4.22]:

$$F_H = \frac{1}{2}\frac{\partial \Lambda}{\partial g_m}(\Delta\Theta)^2 \qquad \text{Equation 4.9}$$

with: $\Lambda = \mu \dfrac{S}{g_m}$ = *magnetic permeance*

$\Delta\Theta = H_x \cdot g_m$ = *magnetic potential variation*

with: H_x = *magnetic field in the x direction* $[Am^{-1}]$

μ = *magnetic permeability* $[V\,s\,A^{-1}m^{-1}]$

S = *cross sectional surface* $[m^2]$

g_m = *air gap [m]*

The calculation of the magnetic field, between the beam and the structure, required to close the switch is determined by equalising the mechanical and the magnetic forces:

$$H_x = \sqrt{\frac{2 \cdot k \cdot g_e}{\mu_0 \cdot S}} \qquad \textit{Equation 4.10}$$

with: μ_0 = *air permeability*$[V\,s\,A^{-1}m^{-1}]$

As the field is propagating in the air gap, the magnetic induction is given by:

$$B_x = \sqrt{\frac{2 \cdot \mu_0 \cdot k \cdot g_e}{S}} \qquad \textit{Equation 4.11}$$

with: $B_x = \mu_0 H_x$

The magnetic flux is then equal to:

$$\Phi_x = B_x \cdot S = \sqrt{2 \cdot \mu_0 \cdot k \cdot g_e \cdot S} \qquad \textit{Equation 4.12}$$

4.4.4. Required permanent magnet and coil magnetic field

The calculation of the required magnetic potential to close the switch is determined with Equation 4.1. The surface S is the cross sectional area of the air gap between the movable beam and the right profiled structure (reluctance Ra_5 on Fig. 4.16). The required magnetic potential is then:

$$\Theta = R_{tot} \cdot \sqrt{2 \cdot S \cdot \mu_0 \cdot k \cdot g_e} \qquad \textit{Equation 4.13}$$

and the corresponding ampere turns value for the coil is:

$$N \cdot I = \Theta \qquad \textit{Equation 4.14}$$

4.4.5. Zero-gap magnetic force

The zero-gap force has been calculated to obtain an estimation of the closed relay contact force. It corresponds to the magnetic force value, for which the movable beam is touching the contact pad.

The magnetic force is given by the Equation 4.9. The air gap magnetic potential variation $\Delta\theta a_5$ is given by:

$$\Delta\Theta a_5 = Ra_5 \cdot \Phi_x \qquad \textit{Equation 4.15}$$

The magnetic force is then equal to:

$$F_H(x) = \frac{1}{2} \cdot \frac{(\Delta\Theta a_5)^2}{Ra_5 \cdot x} \qquad \textit{Equation 4.16}$$

with: x= gap width

The combination of Equation 4.13, Equation 4.14 Equation 4.15 and Equation 4.16 gives:

$$F_H(x) = \frac{1}{2\mu_0 S} \cdot \left(\frac{NI}{R + \frac{x}{\mu_0 S}} \right)^2 \qquad \textit{Equation 4.17}$$

with: S = gap cross-section surface
$R = R_{tot} - Ra_5$

To calculate the zero-gap magnetic force, x has to be replace by $x = g_m - g_e$ (g_m is the initial magnetic gap width and g_e the electric gap width, see Fig. 4.17). The contact force F_{cont} value is then obtained by subtracting the mechanical force F_k (Equation 4.8) to the zero-gap magnetic force.

4.4.6. Calculated value

To calculate the numerical value of the different parameters, the permeability of nickel has to be defined. As it is a ferromagnetic material, the permeability depends on the applied magnetic field and has to be then extracted from magnetisation curves ([4.23] in this case). The required induction field B_x between the movable beam and the contact pad is first calculated from Equation 4.10, the corresponding magnetic field H_x in nickel is then extracted from the curve and the permeability μ is calculated. It has been admitted that μ is constant for the magnetic fields which are involved. The value of μ has been calculated for the switch having a beam length of 1500 µm and is equal to $5.67\ 10^{-4}$ H/m. Table 4.1 shows the summary of different calculated parameters for switches with 1000, 1500 and 2000 µm long beam. The second column is the spring factor of the movable beam (Equation 4.7). The third column is the required induction field (Equation 4.11). The forth column shows the calculated magnetic reluctance (Equation 4.5). It has been assumed that the magnetic field is generated by a source distant of 350 µm from the switch (Ra_1 and Ra_8). The fifth column is the calculated required ampere-turn value (which is also the magnetic potential, Equation 4.13 and Equation 4.14) which has to be generated to close the switch. The last column is the corresponding required number of coil spires for an applied coil current of 30 mA.

Beam length [µm]	k [N/m]	B_x [T]	R_{tot} [H^{-1}]	N*I [A]	Number of spires
1000	4.72	$6.51\ 10^{-2}$	$2.31\ 10^{10}$	21.1	703
1500	1.4	$2.71\ 10^{-2}$	$2.27\ 10^{10}$	14.8	493
2000	0.59	$1.48\ 10^{-2}$	$2.24\ 10^{10}$	11.2	373

Table 4.1: Calculated value for different nickel switch configurations and parameters.

Table 4.2 shows the value of the mechanical force, zero-gap magnetic force and the contact force extracted from the values of Table 4.1.

Parts of the next paragraph compare the theoretical calculation with observations and measured values.

Beam length [µm]	F_k [N]	$F_h(x=g_m-g_e)$ [N]	F_{cont} [N]
1000	$23.6\ 10^{-6}$	$24.2\ 10^{-6}$	$0.6\ 10^{-6}$
1500	$7\ 10^{-6}$	$7.1\ 10^{-6}$	$0.1\ 10^{-6}$
2000	$2.95\ 10^{-6}$	$2.98\ 10^{-6}$	$0.03\ 10^{-6}$

Table 4.2: Calculated value of the mechanical, magnetic and contact forces for different nickel switch configurations.

4.5. CHARACTERISATION

Different simple experiments have been performed to characterise some basic properties of the switch and of the material: electrical resistance, mechanical behaviours and magnetic properties. The comparison of measured values with calculated values is also presented.

4.5.1. Electrical resistance

Closed relay resistance

Electrical resistance values have been obtained by closing the relay with an external permanent magnet (0.1 T, Fig. 4.18) and by measuring the current-voltage curve and calculating the slope (Fig. 4.19). The set-up resistance has been first determined and the switches resistance has been then calculated by subtracting the set-up resistance to the measured values. The measured values correspond then to the switch and the contact resistances.

Fig. 4.18: Picture of the relay and the permanent magnet used to close it.

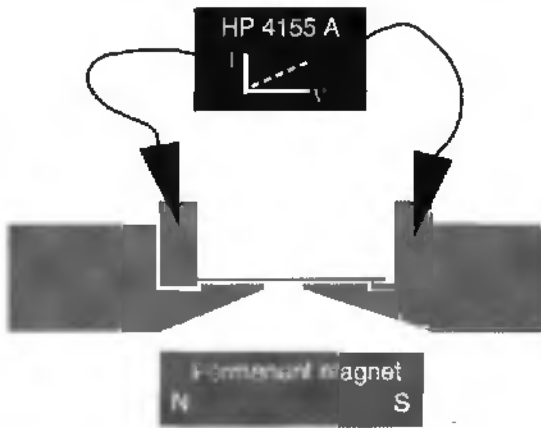

Fig. 4.19: Schematic drawing of the resistance measurements set-up.

The measured current-voltage curve (Fig. 4.20), used to determine the closed relay resistance, has a linear characteristic, except for low voltages. To avoid any structure damages, the current has been limited to 10 mA.

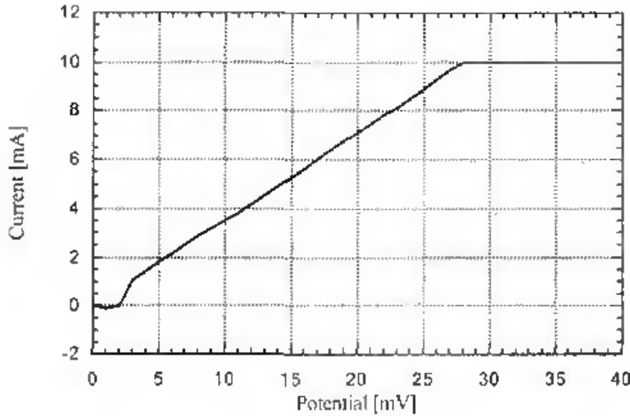

Fig. 4.20: Current-voltage curve of a closed relay. Current has been limited to 10 mA

The Table 4.3 shows the electrical resistance value for different switch configurations. The beams have the same width (14 µm) and the same contact pad/beam gap (4 µm). The electrical resistance of the relays with three different beam lengths and the resistance of the relays with the special geometry to avoid sticking have been measured. The resistance has also been measured for the switches having an electroless deposited gold layer and those having an evaporated silver layer.

Beam length	Nickel	Gold	Silver
1000 µm	2 Ω	8 Ω	10 Ω
1500 µm	2 Ω	9 Ω	11 Ω
2000 µm	2 Ω	8 Ω	10 Ω
1000 µm (special shape pad)	3 Ω	13 Ω	14 Ω

Table 4.3: Measured electrical resistance values for different switch configurations and contact materials.

The beam length has no effect on the electrical resistance, but it strongly determines the position of the magnet needed to close the switch. The shorter is the beam, the larger is the force needed and closer the magnet should be. The relay with the special shape has a small contact area, which explains its higher resistance.

The effect on the contact resistance value of the electroless deposited gold layer and of the evaporated silver layer has not been as expected. For both cases, the measured resistance is higher than for non-coated switches. As the electroless deposition is a chemical reaction, a nickel composite has certainly been generated at the nickel/gold interface, which should have a higher resistivity than pure nickel. But for the evaporated silver layer, this explanation is not suitable. Another interpretation, which is suitable for both metals, is that a nickel oxide has been formed before the metal deposition. The resistance values difference is then explained by the measurement set-up tools. Needles have been used to make the electrical connection between the set-up and the switch. For non-coated switches, the needles have transfixed the fragile nickel oxide layer and the measured resistance value was then corresponding to the desired one. But for coated switches, the deposited metal has acted as a protective layer, the needles have then not transfixed the nickel oxide and the measurement value has been including the metal and the nickel oxide resistances.

The SEM picture on Fig. 4.21 shows a switch with its beam pressed on the contact pad. As side walls are not perfectly vertical, only the top of the beam is contacting the pad. The contact resistance is therefore larger than if the whole beam lateral surface would have made the contact.

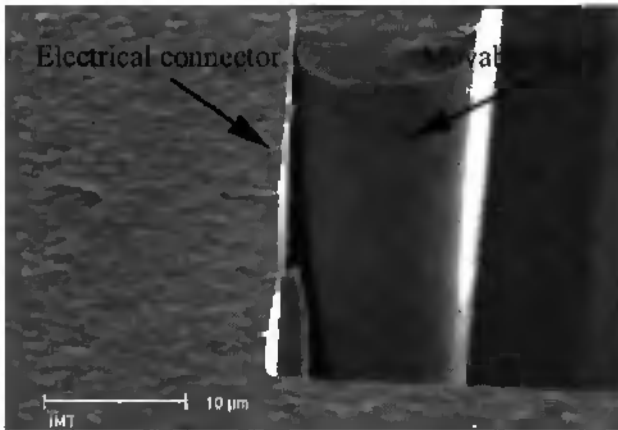

Fig. 4.21: SEM picture of the beam pressed on the contact pad. Only the top of the beam makes the contact with the contact pad.

Open relay resistance

The open relay resistance value has been measured with the same set-up as for the close relay resistance (without approaching the magnet). For potentials up to 100 Volts (upper limit of the set-up tool), the electrical resistance of an open relay has been measured higher than 1 GΩ (limit of the instrument), which indicates a rather low current leakage of the device.

4.5.2. Dynamic measurements

Measurements have also been made to characterise the dynamic behaviour of the switch although it doesn't concern its initial application. The magnetic field has been generated by an external "macro" coil driven with a square signal. An electrical potential has been applied between the electrical ports and the signal has been measured on a resistance placed in between (Fig. 4.22). The coil has been home fabricated with a nail acting as a core. The nail sharpened end has helped to concentrate the magnetic field.

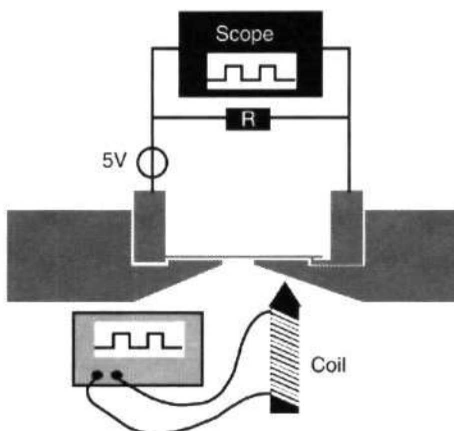

Fig. 4.22: Schema of the dynamic measurements set-up (not to scale).

The graph on the Fig. 4.23 shows the response of the device to an excitation signal oscillating at 10 Hz. The amplitude of the excitation signal and of the measured signal are normalised. The noise appearing during the device open phase is due to the electrical network 50 Hz interference.

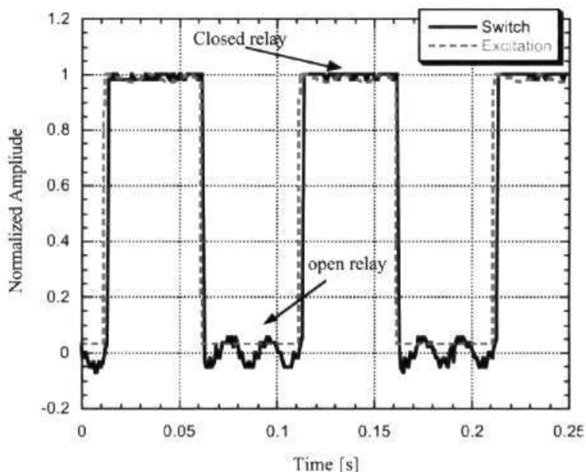

Fig. 4.23: Response of the switch to a square magnetic field at 10 Hz as function of time.

The graph on Fig. 4.24 shows a close view of a 100 Hz cycle. Two phases are observed during the closing of the switch. The first phase is measured to have a delay of 0.2 millisecond (*delay 1*) and the second a delay of 1.6 millisecond (*delay 2*). These two steps are explained by the profile of the beam (Fig. 4.21). The first step corresponds to the connection of the top beam edge and the contact pad and the second step to the connection of the whole beam lateral surface with the contact pad. A 0.4 millisecond delay (*delay 3*) is measured for the opening phase. *Delay 3* is twice *delay 1* duration. This value difference has been generated by the magnetisation of the different ferromagnetic parts (the switch and the coil core), which has induced a remnant force.

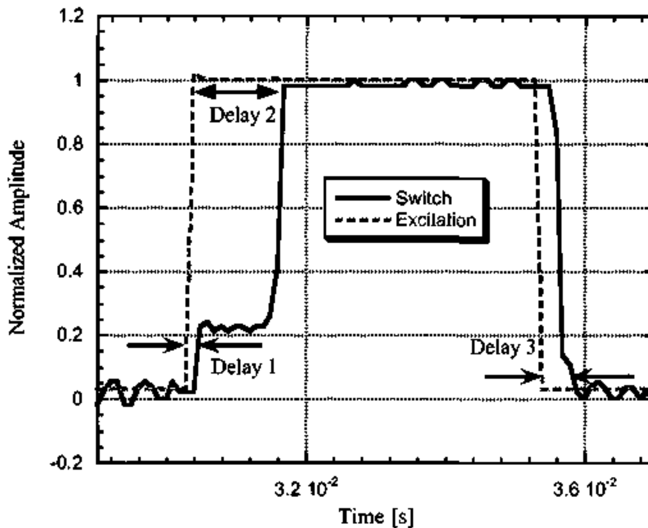

Fig. 4.24: Close view of a cycle of a square excitation at 100 Hz. Two steps are observed for the rising edge.

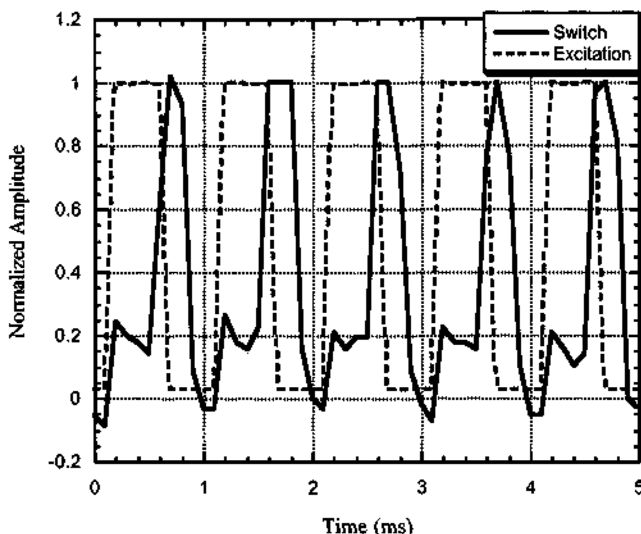

Fig. 4.25: Device response to a 1 kHz square signal.

The relay has successfully been driven up to 1 kHz (Fig. 4.25). This frequency bas been tbe limits reached with the set-up. Two closing steps have also been observed and have been measured. *Delay 1* is about 0.1 millisecond and *delay 2* is 0.5 millisecond. At this frequency, the switch opening *delay 3* has been measured to be 0.3 millisecond long.

4.5.3. Self test coil

The self-test function of the switch has been included to give the opportunity to test the device without the requirement of an external magnetic field. A small coil has been mounted near the device on the SMD package (Fig. 4.26). The fabricated coil* is 3 millimetre long, 0.5 millimetre in diameter, has a copper core and has 400 spires.

* *Fabricated by Sokymat SA, 1614 Granges (Veveyse), Switzerland*

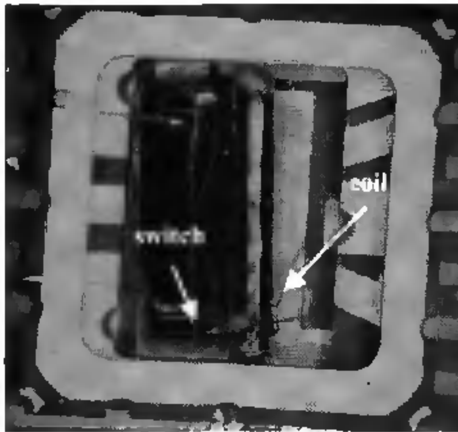

Fig. 4.26: Photograph of the wire-bonded iron-nickel relay and the self-test coil mounted on the SMD package.

The maximal current value of the coil is 30 mA DC and 300 mA AC. The maximum DC ampere-turn value is then 12 and, compared to the calculated value in Table 4.1, should be sufficiently high to close the 2000 μm long beam switch. But for any nickel switches, the magnetic potential delivered by the coil has not been high enough to significantly actuate the movable beam. Tests have also been made with iron-nickel electroplated switches. The movable beam was seen moving, but not closing, when an oscillating signal was driving the coil. The static mode has also been tested and the iron-nickel switch was closed just before the coil overheated.

4.5.4. Permeability

The determination of the material permeability is relatively important for the theoretical calculation. The theoretical switch model consists in magnetic reluctances, which are dependent on the permeability. An extracted permeability value of the nickel magnetisation curve in [4.23] has been used to design the switch. The experiment with the self test-coil indicates that this value seems not to correspond with the electrodeposited nickel value.

Permeability measurement

A simple experiment has been used to obtain an approximation of the electrodeposited nickel or iron-nickel magnetic permeability value. The self-induction coefficient L_{air} of a hollow coil with no core has been measured with an impedance-meter. The experiment has been reproduced with 1,2,...8 electrodeposited nickel (or iron-nickel) samples acting as cores. The total self-induction coefficient L_{tot} has been each time measured. The mean permeability value is then extracted from these measurements. Equation 4.18 to Equation 4.22 describe the analytical calculation concept of this method.

The total coil impedance L_{tot} is express by:

$$L_{tot} = N^2 \cdot \Lambda_{tot} \qquad \textit{Equation 4.18}$$

with N = *Number of coil spires*

$$\Lambda_{tot} = \Lambda_{Ni} + \Lambda_{air} \qquad \textit{Equation 4.19}$$

The magnetic permeances Λ are varying with the number n of nickel (or iron-nickel) samples acting as core and are expressed by:

$$\Lambda_{air} = \frac{\mu_0(A_0 - n \cdot A_{Ni})}{l_0} = L_{air} - \frac{\mu_0 \cdot n \cdot A_{Ni}}{l_0}$$ *Equation 4.20*

$$\Lambda_{Ni} = \frac{\mu_{Ni} \cdot n \cdot A_{Ni}}{l_{Ni}}$$ *Equation 4.21*

with A_0= *coil cross area*
A_{Ni}= *nickel sample cross area*
l_0= *coil length*
l_{Ni}= *nickel sample length*
μ_0= *air permeability*
μ_{Ni}= *nickel permeability*

and the nickel (or iron-nickel) permeability is then expressed by:

$$\mu_{Ni} = (\frac{L_{tot} - L_{air}}{N^2 \cdot n \cdot A_{Ni}} + \frac{\mu_0}{l_0}) \cdot l_{Ni}$$ *Equation 4.22*

The electrodeposited nickel or iron-nickel (50%-50%) samples are 3.5 cm and 2 cm long, 3.7 mm and 2.7 mm wide, and 42 µm and 49 µm thick respectively. The measured self-induction coil coefficient value L_{air} (without nickel bar) is 77 mH. Table 4.4 shows the calculated value of the nickel and iron-nickel permeabilities. The measured electrodeposited nickel permeability is about 25 smaller than the value extracted from [4.23] (which was for pure bulk nickel) but 1.6 higher than the value given in [4.15] (which was for electrodeposited nickel).

Material	Permeability [Vs/Am]
Ni	$2.4\ 10^{-5}$
Fe-Ni	$2\ 10^{-4}$
Ni [4.23]	$5.67\ 10^{-4}$

Table 4.4: Mean iron-nickel and nickel magnetic permeability value calculated with Equation 4.22.

Theoretical and measured values comparison

The permanent magnet (see Fig. 4.18), used to characterise the electrical resistance, generates an induction field of 0.1 T at a distance of 5 mm of its pole. The magnetic potential is estimated to be *398 A*. Compared to the theoretical required value in Table 4.1, the magnetic potential is high enough to close any nickel and iron-nickel switches. This has been confirmed by the experiment.

The experiment with the self-test coil has shown a discrepancy with the calculated values. The model predicted that the magnetic potential generated by the coil should be sufficiently high to close the switch, but it didn't occur. The model calculation has been simplified and did not consider any loss. On the other side, the measured and the literature extracted nickel permeabilities have been observed to be completely different. The required ampere-turn values have been again calculated with the measured magnetic permeabilities. Table 4.5 shows the newly calculated ampere-turn value required to close the switch with the self-test coil. The first row corresponds to the values given in Table 4.1. The second and the third rows are the new values calculated with the measured permeability from Table 4.4. The upper ampere-turn limit of the coil is *12 A*. This new calculation shows that the required ampere-turn to close any nickel fabricated switch is largely higher than the coil upper limit. The 2000 μm long beam iron-nickel switch required value is equal to *12 A*. The new calculated model values are in total agreement with the experimental observations:

- The coil has overheated when the 2000 μm iron-nickel switch closed indicating that the required ampere turn value is close to the upper limit of the coil
- No nickel switch could be closed

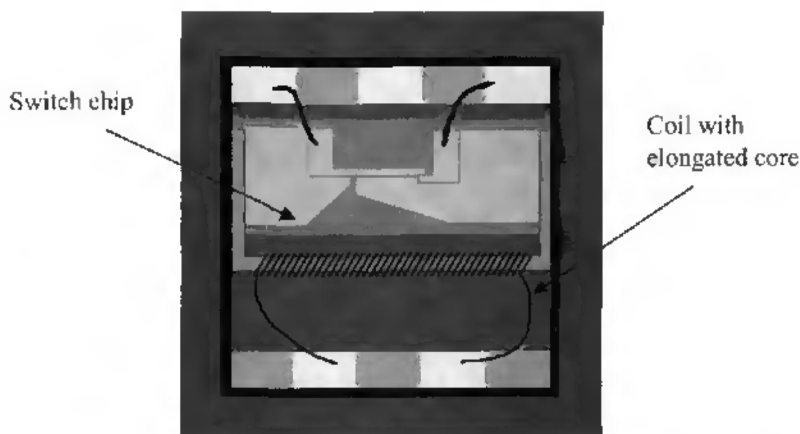

Fig. 4.27: Schematic top view of the SMD packaging with the coil core connected to the switch.

4.6. CONCLUSION

The fabrication of a nickel or iron-nickel electrodeposited reed relay has been demonstrated using a single mask fabrication process. The 55 µm thick photoresist technology has been demonstrated to be fully suitable for that kind of application. Fabrication guidelines for future switch generation have been established. This prototype generation has been successfully tested and has shown to be suitable for static detection with a commercial permanent magnet. Dynamic behaviour has also been tested and the switch has been driven up to 1 kHz. The contact resistance (including the switch resistance) has been measured for different switch designs and metal layer covering. Higher resistance values have been observed for gold or silver covered switches, which lets suppose the presence of nickel oxide between the covering metal layer and the nickel. The open resistance has been measured to be higher than 1 GΩ. The closing and the opening delay have been measured and were found to be mainly due to the magnetic inertia of the experiment set-up. Some predicted design

	1000μm	1500 μm	2000 μm
$\mu_{Ni\ [4.23]} = 5.67\ 10^{-4}$ H/m	21.1 A	14.8 A	11.2 A
$\mu_{Ni} = 2.4\ 10^{-5}$ H/m	41.8 A	31.3 A	22.4 A
$\mu_{Fe\text{-}Ni} = 2\ 10^{-4}$ H/m	22.8 A	14.9 A	12 A

Table 4.5: Calculation of the required ampere-turn value to close the switch with the self-test coil. The measured nickel (μ_{Ni}) and iron-nickel ($\mu_{Fe\text{-}Ni}$) permeabilities have been included in the model.

4.5.5. Design improvements

One major design change, which should improve the self-test function performances, would be to connect physically a coil with a ferromagnetic core to the switch. This connection can be either insured by elongating the coil core (Fig. 4.27) or by integrating a structure on the switch which would act as coil anchorage. Two air gaps would be then suppressed and the magnetic field would be guided to the switch. The required ampere-turn value for a 2000 μm long beam switch of nickel or iron-nickel would be then *12 A* and *1.6 A* respectively.

Another improvement would be to use a meander-like coil, which would occupy the whole available surface (4x5 mm^2). The number of spires and the ampere-turn value would be increased. But the realisation of such an exotic coil would have to resort to a much more complex fabrication process.

effects have been confirmed (e.g. switches with long beam were the most sensitive).

The magnetic permeability has been estimated with a simple measurement method. The obtained value for the electrodeposited nickel is 25 times smaller than the one for bulk nickel [4.23] but 1.6 higher than the one reported in [4.15]. A simple analytical model has allowed to calculate some switch parameters like the required ampere-turn value to close the switch and the total magnetic reluctance. Calculations have been made with permeability values extracted from the literature and from the measurements.

The self-test coil has also been tested but the expected results have not been achieved. The number of ampere-turn was insufficient to close the nickel switch. Only one design of the iron-nickel devices has worked. This misfunctioning has been found to be due to a design error. All the calculations were made with the permeability extracted from [4.23], which was bulk nickel and not electrodeposited nickel value. By introducing the measured permeability values in the model, the cause of the misfunctioning was clearly establisbed. It demonstrated that the analytical calculation has relatively well described the observed measurements. However, this first switch design generation has shown its limitations and some design improvements have been proposed to make the self-test function workable. The working principle has shown to be promising and the fabrication process quite well appropriated for this application.

4.7. REFERENCES

[4.1] M.-A. Grétillat, F. Grétilllat and N. F. de Rooij, "Micromechanical relay with electrostatic actuation and metallic contacts", Technical Digest Transducers '99, pp. 1280-1283, Sendai, Japan.

[4.2] S. Zhou, X. Q. Sun and W. N. Carr, "A monolithic variable inductor network using microrelays with combined thermal and electrostatic actuation", J. Micromech. Microeng. , 9 (1999), pp. 45-50.

[4.3] S. Majumder, N. E. McGruer, P. M. Zavracky, G. G. Adams, R. H Morrison, j. Krim, "Measurements and modelling of surface micromachined electrostatically actuated microswitches, Technical Digest Transducers '97, pp. 1145-1148, Chicago, USA.

[4.4] M. Sakata, Y Komura, T. Seki, K. Kobayashi, K. Sano, S. Horiike, "Micromachined relay which utilises single crystal silicon electrostatic actuator", Proc. MEMS 99, pp. 21-24, Orlando, USA.

[4.5] X. Q. Sun, K. R. Farmer and W. N. Carr, "A bistable microrelay based on two-segment multimorph cantilever actuators", Proc. MEMS 98, pp. 154-159, Heidelberg, Germany.

[4.6] J. A. Wright and Y. C. Tai, "Magnetostatic MEMS relays for the miniaturisation of brushless DC motor controllers", Proc. MEMS 99, pp. 594-599, Orlando, USA.

[4.7] H. A. C. Tilmans, E. Fullin, H. Ziad, M. D. J. Van de Peer, J. Kesters, E. Van Geffen, J. Bergqvist, M. Pantus, E. Beyne, K. Baert and F. Naso, "A fully-packaged electromagnetic microrelay", Proc. MEMS 99, Orlando, USA, pp. 25-30.

[4.8] H. Hosaka, H. Kuwano and K. Yanagiswa, "Electromagnetic microrelays: concepts and fundamental characteristics", Sensors and Actuators A, 40, 1994, pp. 41-47.

[4.9] H. Guckel, T.R. Christenson, K.J. Skrobis, T.S. Jung, J. Klein, K.V. Hartojo, and I. Widjaja, " A first functional current excited planar rotational magnetic micromotor", Proc. MEMS 93, Fort Lauderdale, USA, pp. 7-11.

[4.10] H. Guckel, T. Earles, J. Klein, D. Zook, T. Ohnstein, " Electromagnetic linear actuators with inductive position sensing for microrelay, microvalve and precision positioning applications.", Proc. Transducers'95, Stockholm, Sweden, pp. 324-327.

[4.11] J. Gobet, F. Cardot, "Through mask electroplating applied to the fabrication of microelectromagnet arrays", Proc. of 2nd International Symposium on Electrochemical Microfabrication, Vol. 94-32, Miami, USA, 1994, pp. 130-137.

[4.12] L.J. Guérin, A. Torosdagi, P. Eichenberger, Ph. Renaud " High aspect ratio planar coil embedded in SU8 photoepoxy for MEMS applications", Proc. Eurosensors XII, 1998, pp. 11-14.

[4.13] J.Y. Park, M.G. Allen, "Development of magnetic materials and processing techniques applicable to integrated micromagnetic devices", J. Micromech. Microeng., 8, 1998, pp. 307-316.

[4.14] C. Hang, Y. Kim, M. Allen, " A planar variable reluctance magnetic micromotor with fully integrated stator and wrapped coils", Proc. MEMS 93, Fort Lauderdale, USA, pp. 1-6.

[4.15] B. Rogge, J. Schulz, J. Mohr, A. Thommes and W. Mens, "Fully batch fabricated magnetic microactuators using a two layer LIGA process", Proc. Transducers'95, Stockholm, Sweden, pp. 320-323

[4.16] D. de Bruyker, J.B. Chevrier, K. Baert, R. Puers, H. Löwe, "A silicon micromachined magnetic actuator using a two layer electroplating process", Proc. Actuators 96, Bremen, Germany, 1996, pp. 88-91.

[4.17] V. Seidermann, M. Ohnmacht, S. Büttgenbach, " An optimized multilayer fabrication process for high aspect ratio electromagnetic devices and microsystems", Proc. Transducers'99, Sendai, Japn, 1999, pp 102-105.

[4.18] E. Fullin, J. Gobet, H. Tilmans, J. Berqvist, "A new basic technology for magnetic micro-actuators", Proc. MEMS 98, Heidelberg, Germany, pp. 143-147.

[4.19] H. Miyajima and M. Mehregany, " High-aspect-ratio photolithography for MEMS applications", J. of Micromechanical Systems, Vol. 4, No. 4, 1995, pp. 220-229.

[4.20] M. Jufer, "Transducteurs électromécaniqes", Traité d'électricité, vol. IX, presses polytechniques romandes, Lausanne, 1985, chapitres. 1 & 2.

[4.21] W. C. Young, "Roark's Formulas for Stress & Strain", 6th ed., McGraw-Hill International Editions, New York, 1989, chap. 7.

[4.22] J. D. Kraus, "Electromagnetic", McGraw-Hill Company, Inc, New York, 1953, Chap. 15.

[4.23] Metals Handbook, Vol. 1, "Properties and selection of metals", 8th edition, American Society for Metals, p. 792.

Chapter 5
Conclusion

Thick resist process

The thick resist moulds fabrication processes, which have been developed, have been demonstrated to be suitable for MEMS devices fabrication. They have demonstrated, for certain applications, to be a good and low cost alternative to LIGA process. With the proposed fabrication techniques, high aspect ratio metallic structures have been easily fabricated with conventinal IC tools. The optimised resist mould processes have proven to be very reproducible and allow the fabrication of 38 μm, 55 μm and 85 μm thick resist mould with a yield close to 100%. Process limitations and requirements have been determined and guide lines for the design of MEMS processes have been established.

The influence of each fabrication step on the moulds quality and resolution has been explained and particularly, the rehydration time parameter has been highlighted to be very important. The thick resist fabrication process has shown to be a very critical technology, which has to be finely "tuned". Any deviation from the optimised parameters value, including the room humidity and temperature, has proven to be compromising for the fabrication success.

Applications

Chapter 3 demonstrated that the thick resist technology is not limited to the fabrication of moulds for metal electrodeposition but also, for example, can be used as a protective layer of protruding structures during wet and dry etching experiments. Different devices have also been reported, which have included in their fabrication process the developed thick resist layer photopatterning process.

The fabrication of a nickel electrodeposited gyroscope has demonstrated the suitability of the thick resist technologies for MEMS applications. Useful information on the fabrication, design, simulation and characterisation of an electrostatic actuator have been obtained.

Chapter 4 demonstrated that the electrodeposited nickel is also suitable for the realisation of devices for magnetic applications. A reed relay, for position detection applications, has been successfully fabricated and tested. The main advantages of the proposed design are the simplicity of the fabrication process, which required a single photolithography step, and the small size of the device. The characterisation of the relay has allowed to highlight some design errors and to adjust the parameters of the proposed theoretical analytical model. Some improvements for future switch generations have been proposed.

And then...

The main goal of this thesis work was to demonstrate the suitability of thick resist layer photopatterning for MEMS applications. Thick photoresist technology has shown the wide range of possible applications in the world of microfabrication. Combination with other microfabrication techniques, as it was done with Su-8, is an opened direction, which should be investigated. The author would like to convince the reader that even if the thick resist photopatterning is a critical technology, the presented results should encourage him to make use of this technique in future device fabrication.

Acknowledgements

This work would not have been possible without the help of a lot of people, some of which I would mention here.

First of all, I would like to thank Prof. Nico de Rooij who gave me the opportunity to work in his group for four years. Thank you for encouraging me during all this time !

Special thanks also to Prof. Milena Koudelka-Hep for accepting to be co-examiner of this thesis and for answering to my chemistry related questions.

Part of this work has been realised in collaboration with the Swiss Center for Electonics and Microtechnology (CSEM). I would like to acknowledge François Crevoisier for the electrodeposition of Fe-Ni layers, Jean Gobet for discussions about thick resist and nickel electroplating technologies, and Dr. Jean-Marc Moret for reading and correcting this thesis. Further, I thank Dr. Johan Bergqvist for having kindly agreed to be co-examiner for this thesis.

Special thanks belong to Jean-Marc Tapernoux for correcting the *franglais* of this manuscript.

I would like to thank the technical staff (Sylvain Jeanneret, Sabina Jenny, José Vaquera and Gianni Monding (*lui è il migliore*)) for their support and especially Pierre-André Clerc for the electrodposition of nickel layers and for all the non- and professional discussions (*smör!*), and Sylviane Pochon for the

dicing, the packaging, the wire bonding, the soldering (*elles étaient si petites ces bobines*) *et tout le reste (miam miam…)*.

Thank you Florence Grétillat and Pierre Thiébaud for introducing me to the cleaning room behaviour. Thank you Marc-Alexis Grétillat for your help during the gyro's conception.

Special thanks goes to Peter van der Wal for answering to all my questions about chemistry and for speaking with me so well the *smör sö sö* language…

I would like to thank, Terunobu Akiyama, the Grétillat family, Antoine Daridon and Eva L'Hostis, with whom I shared the same office, for the pleasant atmosphere during these years.

I would like to thank also Marco (*dropmix supplier*), Philippe (*tovaritch*), Philippe (*the Français*), Philippe (*von Holz*), Beny from Ropongi, Danick the Canadien !, Urs the Bear, Georges (*Bill best friend*), Cynthia (humm les truffes), Olivier-san, the *???* team (Seb, Gian and Arash), the computer team Matthias, Christophe and Claudio, and all the other collaborators of the Samlab group.

Very special thanks to the KTS Corporation (i.e Bastien, Honoré PFI Désiré, Greg the *mille-feuilles* tester and Pellimou the *hargneux*) for the psychological support during all this time.

Merci Christine pour ton support, ton aide et ta compréhension pendant toute la durée de ma thèse. Et merci à toi Alexia d'avoir voulu, si souvent, m'aider à rédiger ce manuscrit… Un grand merci à mes parents qui m'ont permis de faire des études. Merci à tous de votre soutien !

Bibliography

Refereed Articles :

M.-A Grètillat, F. Paoletti, P. Thiébaud, S. Roth, M. Koudelka-Hep and N.F. de Rooij, "A New Fabrication Method for Borosilicate Glass Capillary Tubes with Lateral Inlets and Outlets", Sensors & Actuators, A60 (1997), pp. 219-222, 1997

L. Dellmann, S. Roth, C. Beuret, L. Paratte, G.-A. Racine, H. Lorenz, M. Despont, P. Renaud, P. Vettiger, N. F. de Rooij, "Two steps micromoulding and photopolymer high-aspect ratio structuring for applications in piezoelectric motor components", Microsystem Technologies, vol. 4, no. 3, pp. 147-150, 1998

L. Dellmann, S. Roth, C. Beuret, G.-A. Racine, H. Lorenz, M. Depont, P. Renaud, P. Vettiger, N. F. de Rooij, "Fabrication process of high aspect ratio elastic and SU-8 structures for piezoelectric motor applications", Sensors and Actuators, A Physical, vol. 70, pp. 42-47, 1998

P.-F. Indermuhle, S. Roth, L. Dellmann, N.F. de Rooij, "Patterned thick photoresist layers for protection of protruding structures during wet and dry etching processes", Journal of Micromechanics and Microengineering, vol. 8, no. 2, pp. 74-76, 1998

P.-A. Clerc, L. Dellmann, F. Grétillat, M.-A. Grétillat, P.-F. Indermühle, S. Jeanneret, Ph. Luginbuhl, C. Marxer, T.L. Pfeffer, G.-A. Racine, S. Roth, U. Staufer, C. Stebler, P. Thiébaud, N.F. de Rooij, "Advanced deep reactive ion etching: a versatile tool for micromechanical systems", Journal of Micromechanics and Microengineering, vol. 8, pp. 272-278, 1998.

S. Roth, L. Dellmann, G.-A. Racine, N.F. de Rooij, "High aspect ratio UV photolithography for electroplated structures", Journal Micromechanical Microengineering, vol. 9, pp. 105-108, 1999

Conference and Workshop Papers :

M.A. Grétillat, F. Paoletti, P. Thiébaud, S. Roth, M. Koudelka-Hep, N.F. de Rooij, "A New Fabrication Method of Borosilicate Glass Capillary Tubes with Laterial Inlets and Outlets", Proceedings of Eurosensors X, The 10th European Conference on Solid-State Transducers, Leuven, Belgium, pp. 259-262, September 1996

M.-A Grétillat, F. Paoletti, P. Thiébaud, S. Roth, M. Koudelka-Hep and N.F. de Rooij, "A New Fabrication Method of Borosilicate Glass Capillary Tubes with Lateral Inlets and Outlets", Proceedings of Miniaturized Total Analysis Systems, µ-TAS96, Analytical Methods & Instrumentation, Basel, Switzerland, p. 214, November 1996.

L. Dellmann, S. Roth, C. Beuret, G.-A. Racine, H. Lorenz, M. Despont, P. Renaud, P. Vettiger, N.F. de Rooij, "Fabrication Process of High Aspect Ratio Elastic Structures for Piezoelectric Motor Applications", Digest of Technical Papers of the 9th Internat. Conf. on Solid-State Sensors & Actuators, TRANSDUCERS '97, Chicago, USA, pp. 641-644, 1997

P.-F. Indermuhle, L. Dellmann, S. Roth et N.F. de Rooij, "Patterned Thick Photoresist Layers for Protection of Protruding Structures During Wet and Dry Etching Processes", Proc. Micromechanics Europe '97, Southampton, UK, pp. 39-42, 1997

S. Roth, L. Dellmann, G.-A. Racine, N.F. de Rooij, " High aspect ratio UV photolithography for electroplated structures", Proc. Micromechanics Europe '98, Ulvik, N, pp. 55-58, 1998

S. Roth, C. Marxer, G. Feusier, N. F. de Rooij, "One mask nickel micro-fabricated reed relay", Proceedings of the 13th IEEE Workshop on Micro Electro Mechanical Systems, MEMS'2000, Miyazaki, Japan, pp. 176-180, January 2000.